







Disentangling the formation history of galaxies via population-orbit superposition: method validation

Ling Zhu¹ , ¹★ Glenn van de Ven² , ² Ryan Leaman³, ³ Robert J. J. Grand⁴ , ⁴ Jesús Falcón-Barroso^{5,6}, ^{5,6} Prashin Jethwa², ² Laura L. Watkins⁷ , ⁷ Shude Mao⁸, ⁸ Adriano Poci^{9,10} , ^{9,10} Richard M. McDermid⁹ and Dylan Nelson⁴ 

¹Shanghai Astronomical Observatory, Chinese Academy of Sciences, 80 Nandan Road, Shanghai 200030, China

²Department of Astrophysics, University of Vienna, Türkenschanzstrasse 17, A-1180 Wien, Austria

³Max Planck Institute for Astronomy, Königstuhl 17, D-69117 Heidelberg, Germany

⁴Max-Planck-Institut für Astrophysik, Karl-Schwarzschild-Strasse 1, D-85748 Garching, Germany

⁵Instituto de Astrofísica de Canarias, C/ Via Lactea, s/n, E-38205 La Laguna, Tenerife, Spain

⁶Departamento de Astrofísica, Universidad de La Laguna, E-38200 La Laguna, Tenerife, Spain

⁷AURA for ESA, Space Telescope Science Institute, 3700 San Martin Drive, Baltimore, MD 21218, USA

⁸Physics Department and Tsinghua Centre for Astrophysics, Tsinghua University, Beijing 100084, China

⁹Astronomy, Astrophysics, and Astrophotonics Research Centre, Department of Physics and Astronomy, Macquarie University, Sydney, NSW 2109, Australia

¹⁰European Southern Observatory, Karl-Schwarzschild-Strasse 2, D-85748 Garching bei München, Germany

Accepted 2020 June 1. Received 2020 May 31; in original form 2020 March 15

ABSTRACT

We present population-orbit superposition models for external galaxies based on Schwarzschild's orbit-superposition method, by tagging the orbits with age and metallicity. The models fit the density distributions, kinematic, and age and metallicity maps from integral field unit (IFU) spectroscopy observations. We validate the method and demonstrate its power by applying it to mock data, similar to those obtained by the Multi-Unit Spectroscopic Explorer (MUSE) IFU on the Very Large Telescope (VLT). These mock data are created from Auriga galaxy simulations, viewed at three different inclination angles ($\vartheta = 40^\circ, 60^\circ, 80^\circ$). Constrained by MUSE-like mock data, our model can recover the galaxy's stellar orbit distribution projected in orbital circularity λ_z versus radius r , the intrinsic stellar population distribution in age t versus metallicity Z , and the correlation between orbits' circularity λ_z and stellar age t . A physically motivated age–metallicity relation improves the recovering of intrinsic stellar population distributions. We decompose galaxies into cold, warm, and hot+counter-rotating components based on their orbit circularity distribution, and find that the surface density, velocity, velocity dispersion, and age and metallicity maps of each component from our models well reproduce those from simulation, especially for projections close to edge-on. These galaxies exhibit strong global age versus σ_z relation, which is well recovered by our model. The method has the power to reveal the detailed build-up of stellar structures in galaxies, and offers a complement to local resolved, and high-redshift studies of galaxy evolution.

Key words: methods:numerical – galaxies: formation – galaxies: kinematics and dynamics – galaxies: structure.

1 INTRODUCTION

Stellar dynamics provides a fossil record of the formation history of galaxies. Stars that were born and remain in quiescent environments tend to be on regular rotation-dominated orbits. On the other hand,

stars born from turbulent gas or that have been dynamically heated after birth will be on warmer orbits with more random motions (Leaman et al. 2017). Stellar heating mechanisms include violent mergers (e.g. Benson et al. 2004; House et al. 2011; Few et al. 2012; Helmi et al. 2012; Ruiz-Lara et al. 2016) and long-term secular heating of the disc via internal instabilities (e.g. Jenkins & Binney 1990; Aumer, Binney & Schönrich 2016; Grand et al. 2016).

* E-mail: lzhu@shao.ac.cn

As the Universe evolves, a galaxy’s mass density, gas fraction, and star formation all decrease. This likely reduces the velocity dispersion of the gas from which stars form, the mass spectrum of dense giant molecular clouds, and the frequency of mergers (Genzel et al. 2011; Wisnioski et al. 2015). Stellar kinematics is therefore expected for multiple reasons to be systematically correlated with stellar ages (Trayford et al. 2019). Several observations have revealed that old stars dominate the light of random-motion-dominated bulges, while younger stars live on thinner discs. Stars born during the same epoch tend to live on similar orbits (e.g. Bird et al. 2013; Stinson et al. 2013). At the present day, the stellar phase-space distribution of a galaxy is thus a combination of stars formed over its lifetime. A mixture of merging events and star formation episodes determines the diversity of a galaxy’s structure and stellar populations.

Observationally, it is difficult to identify coherent structures in the density distribution and kinematics of stars formed at high redshift (van der Wel et al. 2016). Fortunately, the chemistry and age imprinted in a star provide coordinates of the time and environment of its birth. Taking the Milky Way (MW) as an example, the chemical abundance and the 6D phase-space information of a single star could be obtained by combining *Gaia* (Gaia Collaboration et al. 2018) and spectroscopic surveys. In the solar neighbourhood, most stars are disc stars, which we can identify as they are on near-circular orbits, and are both young and metal rich (e.g. Mackereth et al. 2017). Although spatially coincident, we can also identify a small fraction of halo stars as they are on radial/vertical-motion-dominated orbits, and are old and metal poor (e.g. Belokurov et al. 2018, 2020; Helmi et al. 2018). The chemical information of disc stars and halo stars gives us insight into the formation history of the MW (Belokurov et al. 2018; Helmi et al. 2018; Fattahi et al. 2019).

However, only a handful of galaxies are near enough for us to resolve their stars. For most external galaxies, all of our information comes from integrated light. In these cases, the spectrum we observe at each pixel is a light-weighted combination of spectra from all the stars along the line of sight, which come from different populations with different ages, metallicities, and kinematics. By full spectrum fitting (e.g. Cappellari 2017), we can obtain the line-of-sight velocity distribution (LOSVD), which is usually described by a Gauss–Hermite (GH) profile with parameters of velocity (V), velocity dispersion (σ), and/or higher order GH coefficients, like the third and fourth order h_3 and h_4 or even higher h_5 and h_6 .

These full spectrum fits also return the average age and metallicity of the underlying stellar populations. Such methodologies have been applied in many integral field unit (IFU) spectroscopic surveys, such as the Calar Alto Legacy Integral Field Area (CALIFA) survey (Sánchez et al. 2012), the Sydney AAO Multi-object Integral Field (SAMI) galaxy survey (Croom et al. 2012), and the Mapping Nearby Galaxies at APO (MaNGA) survey (Bundy et al. 2015). These surveys provide a spectrum at each pixel across the galaxy plane. From these spectra and the aforementioned techniques, we obtain kinematic maps ($V, \sigma, h_3, h_4, \dots$), as well as age and metallicity maps.

Disentangling the different stellar populations in present-day galaxies, and the structures they form, will give us insight into the galaxy’s formation history; however, this is challenging as it typically requires resolved stellar abundances and ages or deep integrated light spectroscopy (Leaman, VandenBerg & Mendel 2013; Boecker et al. 2020). Full spectrum (or spectral energy distribution, SED) fitting has been pushed to provide not only average stellar population properties, but also a distribution of

ages and metallicities – such as a star formation history (SFH) or age–metallicity relation (AMR; e.g. Cid Fernandes et al. 2005; McDermid et al. 2015; Cappellari 2017; Carnall et al. 2019; Leja et al. 2019). Based on the SFH obtained at each pixel, galaxies can be decomposed into structures with different stellar ages and metallicities (Guérou et al. 2016; Pizzella et al. 2018; Pinna et al. 2019a,b; Tabor et al. 2019).

Dynamical models offer us an alternative and powerful tool to probe a galaxy’s formation history. The particle-based made-to-measure method (M2M; de Lorenzi et al. 2007; Long & Mao 2010; Hunt & Kawata 2014) and the orbit-based Schwarzschild method (van der Marel & Franx 1993; Rix et al. 1997; Cretton & van den Bosch 1999; Gebhardt et al. 2000; Valluri, Merritt & Emsellem 2004; van den Bosch et al. 2008; van de Ven, de Zeeuw & van den Bosch 2008; Vasiliev & Valluri 2020) probe how stars orbit in a gravitational potential without ad hoc assumptions about the underlying orbital structures. The triaxial Schwarzschild model developed by van den Bosch et al. (2008) has proved to be effective at recovering the orbit distributions of a variety of galaxies (Zhu et al. 2018a,b; Jin et al. 2019). It has notably been applied to a large sample of 300 CALIFA galaxies in the local Universe to recover their stellar orbit distributions (Zhu et al. 2018b). However, the orbits recovered in that study (and most others) are monochromatic and provide no information about the underlying stellar populations.

Recently, there have been a few pioneering works that have moved beyond this monochromatic view by tagging particles or orbits in dynamical models with a characteristic chemistry or age indicator. These works include a chemodynamic M2M model of the MW bulge (Portail et al. 2017), and both M2M (Long 2016) and Schwarzschild (Long & Mao 2018) chemodynamic models of four nearby galaxies. However, the power and limitations of these methods have not been characterized by testing against mock data. This is what we set out to do here.

Starting from the Schwarzschild code developed by van den Bosch et al. (2008), we arrive at a new population-orbit superposition method. Under the assumption that stars on the same orbit were born close in space and time, we tag each orbit in the Schwarzschild model with an age and metallicity. Thus if we imagine observing the model as we would in a real galaxy, we can predict not only the kinematic distribution along the line of sight, but also the age and metallicity properties as well. In this way, stellar populations at different positions are connected by the underlying orbits, providing a holistic model of the galaxy. A rather similar approach was recently applied to an edge-on galaxy, NGC 3115 (Poci et al. 2019), which offers a tantalizing view into the power of the method by providing the global stellar age versus dispersion (σ_z) relation in an external galaxy.

In this paper, we validate our population-orbit superposition method and demonstrate its power in recovering dynamical structures of different stellar populations by using MUSE-like mock data created with a range of projections from a variety of simulated galaxies. The paper is organized in the following way: in Section 2, we describe the mock data created from the simulations; in Section 3, we describe the method; in Section 4, we illustrate the model recovery of intrinsic orbit distribution, stellar population distribution, and the correlation in between for each galaxy; and in Section 5, we illustrate the orbital decomposition of the galaxies and show the recovery of the age and metallicity properties of different components. We discuss the results in Section 7, and summarize in Section 8.

Table 1. The three simulated galaxies from Auriga project. From left to right: the galaxy name, stellar mass M_* , neutral hydrogen mass $M_{\text{H I}}$ (Marinacci et al. 2017), dark matter (DM) halo mass M_{200} , stellar particle resolution $M_{\text{StarParticle}}$, DM particle resolution $M_{\text{DMParticle}}$ in unit of solar mass M_\odot , Hubble types and specific properties, and the inclination angles (ϑ in degree) projected with for creating mock data sets.

Name	M_*	$M_{\text{H I}}$	M_{200}	$M_{\text{StarParticle}}$	$M_{\text{DMParticle}}$	Type	ϑ ($^\circ$)
Au-5	6.7e10	7.2e9	1.2e12	$\sim 5e4$	$\sim 3e5$	Spiral: spiral arms, weak bar	40, 60, 80
Au-6	4.75e10	1.5e10	1.0e12	$\sim 5e4$	$\sim 3e5$	Spiral: spiral arms, weak bar	40, 60, 80
Au-23	9.02e10	1.45e10	1.6e12	$\sim 5e4$	$\sim 3e5$	Spiral: warps, strong bar	40, 60, 80

2 MOCK DATA

2.1 Simulations

The simulations used for our study are taken from the Auriga project (Grand et al. 2017, 2019), which is a suite of 40 cosmological magnetohydrodynamical simulations for the formation of the MW-mass haloes. These simulations were performed with the AREPO moving-mesh code (Springel 2010), and follow many important galaxy formation processes such as star formation, a model for the ionizing ultraviolet (UV) background radiation, a model for the multiphase interstellar medium, mass loss and metal enrichment from stellar evolutionary processes, energetic supernovae and active galactic nuclei (AGN) feedback, and magnetic fields (Pakmor et al. 2017). We refer the reader to Grand et al. (2017) for more details. In this study, we select three galaxies from the Auriga simulation suite at a mass resolution of $\sim 5 \times 10^4 M_\odot$ for baryons, the typical number of stellar particles is thus $\sim 1\text{--}2 \times 10^6$. The comoving gravitational softening length for the star particles and high-resolution dark matter particles is set to $500 h^{-1}$ cpc. The physical gravitational softening length grows with the scale factor until a maximum physical softening length of 369 pc is reached. This corresponds to $z = 1$, after which the softening is kept constant. The details of which are listed in Table 1.

2.2 Mock data

From each simulation, we take three projections with inclination angles of $\vartheta = 80^\circ, 60^\circ, 40^\circ$ (from edge-on to face-on). Then, we create a mock data set for each projection, thus we have $3 \times 3 = 9$ mock galaxies in total. Au-6 $\vartheta = 80^\circ$ is taken to illustrate the method throughout the paper.

The mock data are created as follows. We first project a simulation to the observational plane with inclination angle ϑ ($80^\circ, 60^\circ, 40^\circ$), and place it at distance $d = 30$ Mpc, then observe it with pixel size of 1 arcsec (1 arcsec = 145 pc). Then we calculate the stellar mass of particles in each pixel to obtain a surface mass density map. According to the number of particles in each pixel, we then perform a Voronoi binning process to reach a target signal-to-noise ratio of $S/N_T = 50$, assuming Poisson noise $\sim \sqrt{N_{\text{particles}}}$. Given all the particles in each Voronoi bin, we derive the mass-weighted velocity, dispersion, h_3 , and h_4 by fitting a GH function (Gerhard 1993; van der Marel & Franx 1993) to the stellar LOSVD, as well as calculate mass-weighted average age (t) and metallicity (Z/Z_\odot). Note that here the velocity and dispersion are not actually the mean velocity and velocity dispersion directly calculated from the LOSVD, but the parameters of the base Gaussian in the GH function.

After the Voronoi binning, the spatial resolution of our mock data is $\sim 150\text{--}1000$ pc. Considering the softening length of 369 pc for star particles in the simulation, the actual spatial resolution is $\sim 400\text{--}1000$ pc, which is comparable, but slightly lower than that of the kinematic data (binned with target single-to-noise ratio $S/N_T =$

100) from the Fornax 3D project (Sarzi et al. 2018). We use a simple function inferred from the CALIFA data to construct the errors for kinematic maps (Tsatsi et al. 2015), with the errors proportional to $\frac{S/N_T}{S/N_{\text{bin}}} (1 + 1.4 \log N_{\text{pix}})$, where $S/N_{\text{bin}} = \sqrt{N_{\text{particles}}}$, and N_{pix} is the number of pixels in a Voronoi bin. We will have larger errors for kinematics in the area with lower surface density, where more pixels are included in each bin in order to reach the target S/N_T . For age and metallicity, the observational errors are more complicated. Tests on full-spectrum fitting to mock spectra of $S/N_T = 40$ obtained random errors of 10 per cent for age and metallicity (Pinna et al. 2019b), the errors could be lower for spectra with higher S/N , while it could be higher for real spectra due to possible systematic effects. For this proof-of-concept we adopt relative errors of 10 per cent for age and metallicity. The kinematics and age and metallicity maps are then perturbed by random numbers, normally distributed with dispersions equal to the observational errors. The error maps of the mock data are similar to the data of MUSE observations for galaxies in the Fornax 3D project (Sarzi et al. 2018).

The mock data created from the simulation Au-6 with $\vartheta = 80^\circ$ are shown in Fig. 1. From left to right, they are stellar velocity V , velocity dispersion σ , GH coefficients h_3 and h_4 , and age and metallicity maps. The first row is the perturbed data and the second row is the corresponding error maps.

For real galaxies, the kinematic maps obtained from observations are usually light-weighted. In that case, we typically measure light-weighted age and metallicity maps, and use surface *brightness* as the tracer density for consistency. Orbits in the model should be interpreted as light-weighted. Here, however, the mock kinematics and age and metallicity maps are mass-weighted so that we use surface *mass* density – rather than surface *brightness* – as the tracer density distribution. Therefore, the orbits in the model are mass-weighted. For method validation, mass-weighted or light-weighted data do not make any difference.

3 METHOD

In this section, we describe how we fit the stellar kinematic maps and the age and metallicity maps with a population-orbit superposition method. The model will proceed as a two-step process: first, fitting the kinematics maps with a standard Schwarzschild’s orbit-superposition model to obtain the orbit weights; second, tagging the orbits with age and metallicities and fitting the age and metallicity maps to obtain the best-fitting age and metallicity of the orbits.

3.1 Schwarzschild method

The three main steps to build a Schwarzschild model are as follows: (1) create a suitable model for the underlying gravitational potential; (2) calculate a representative library of orbits within the gravitational potential; and (3) find the combination of orbits (solve the orbit weights) that match the observed kinematic maps and luminosity/mass distribution of the tracers.

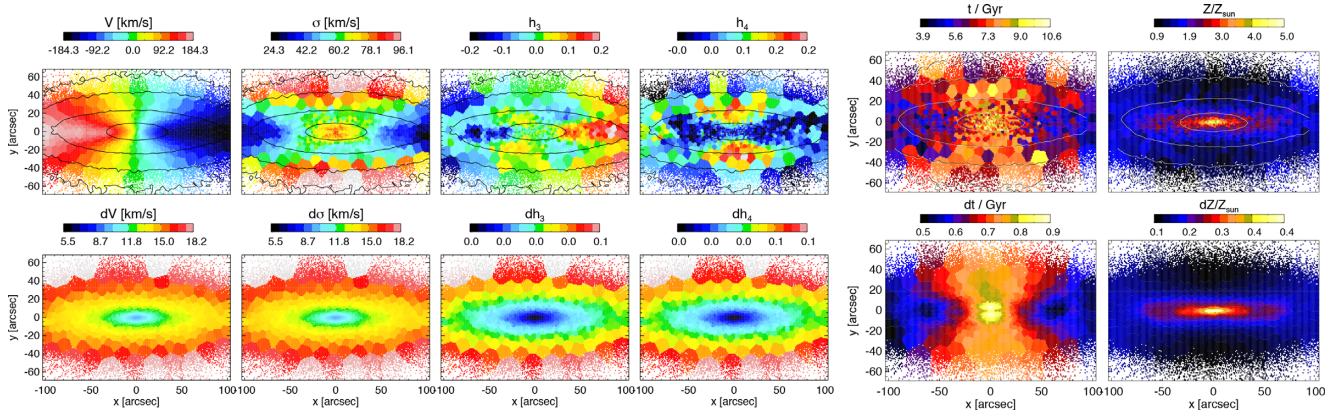


Figure 1. MUSE-like mock data created from the simulation Au-6, projected with inclination angle of $\theta = 80^\circ$. The six columns from left to right are velocity V , velocity dispersion σ , GH coefficients h_3 and h_4 , and age and metallicity maps. The first row is perturbed data, the second row is errors (dt and dZ are 10 per cent of the original unperturbed data). The overplotted contours represent the surface mass density.

The gravitational potential is constructed by a combination of stellar mass distribution and dark matter halo. We deproject the surface brightness to 3D luminosity density by assuming a set of viewing angles (θ, ϕ, ψ). Here θ and ϕ define the orientation of line of sight with respect to the principle axis of the object. The angle ψ is required to specify the rotation of the object around the line of sight.

By multiplying the surface brightness by a stellar mass-to-light ratio, we obtain the intrinsic stellar mass density. Here for the mock galaxies, we actually use surface mass density, instead of surface brightness, to construct the gravitational potential. We still allow for a scale parameter α_{star} , which is analogous to a mass-to-light ratio, but with a true value of 1, to be a free parameter.

A multi-Gaussian expansion (MGE) is used for modelling the surface density and deprojection to 3D density for the stellar component (Emsellem, Monnet & Bacon 1994; Cappellari 2002). For our galaxies close to axisymmetric, we always align the projected major axis with long x -axis on the observational plane and do not allow for a twist between the different Gaussians, thus ψ is always close to 90° .

We use the parameters describing intrinsic shapes ($q = Z/X$, $p = Y/X$, $u = \sigma_{\text{obs, major}}/\sigma_{\text{intr, major}} = x/X$) of the Gaussians, instead of the three viewing angles as free parameters. X , Y , and Z are the intrinsic major, intermediate, and long axis of the galaxy, u is the ratio between σ of observed long axis to the intrinsic long axis. We further fix $u = 0.9999$, while p and q are left free. Note that the intrinsic shape is determined by p and q , thus triaxiality of the stellar component is still allowed in our model. In our case fixing $u = 0.9999$ restricts ϕ in a small region close to 90° and $\sigma_{\text{intr, major}}$ close to $\sigma_{\text{obs, major}}$.

The dark matter is assumed to be a spherical Navarro–Frenk–White (NFW) halo, with concentration C fixed according to M_{200} versus C correlation of Dutton & Macciò (2014).

In summary, we have four free parameters describing the gravitational potential: the scale parameter of stellar mass α_{star} (comparable to a stellar mass-to-light ratio), intrinsic shape parameters p and q , and dark matter virial mass M_{200} .

The method of orbit library sampling and model fitting follow exactly as described in Zhu et al. (2018b) and van den Bosch et al. (2008), which we do not repeat here. It should be emphasized that we do not fit V , σ maps directly, but rather the LOSVD expanded in GH coefficients h_1, h_2, h_3 , and h_4 to solve the orbit weights.

However, we extract V and σ maps from the model at the end for direct comparison to the observational data. By exploring the free parameters describing the gravitational potential, we find the best-fitting model that reproduces the observed stellar kinematic maps and mass distribution.

We characterize the orbits with two parameters: time-averaged radius r and circularity λ_z . Following Zhu et al. (2018b), λ_z is defined as the angular momentum L_z normalized by the maximum that is allowed by a circular orbit with the same binding energy. All quantities are taken as average of the particles sampled along the orbit over equal time interval. The stellar orbit distribution of a galaxy is described as the probability density distribution in the phase space of λ_z versus r . Fig. 2 illustrates the orbit distribution of a typical spiral galaxy. Darker colour indicates higher probability; the total weight of the orbits has been normalized to unity.

The orbit library consists of a few thousand orbits, and a few hundred of them gain significant weights at the end. To reduce the noise in fitting age and metallicity maps, we perform a Voronoi binning in the phase-space r versus λ_z , and divide the orbits into $N_{\text{bundle}} \sim 100$ bundles. Orbits with similar r and λ_z are included in the same bundle, to ensure each bundle has a minimum of orbit weight of 0.005. The resulting binning scheme is shown as the red polygons in Fig. 2.

3.2 Tagging stellar orbits with stellar populations

The observed age map presents values of age, t_{obs}^i , at each aperture i on the observational plane, with a total number of N_{obs} apertures. Throughout the paper, one aperture indicates one spatial bin on the observational plane that may include a few pixels. After dividing the orbits into N_{bundle} bundles (Fig. 2), we resample particles from these orbits in each bundle, by recalculating each orbit and adopting particles along the orbit trajectory with the number of particles drawn from each orbit proportional to its orbit weight. Then we add up all the particles sampled from each orbit bundle, project them to the observational plane, and calculate the mass f_k^i (mass for mass-weighted and flux for light-weighted models) contributed by the orbital bundle k at each aperture i .

This orbit bundle k is tagged with a single value of age t_k . The average value of age in each aperture i is a linear average of the

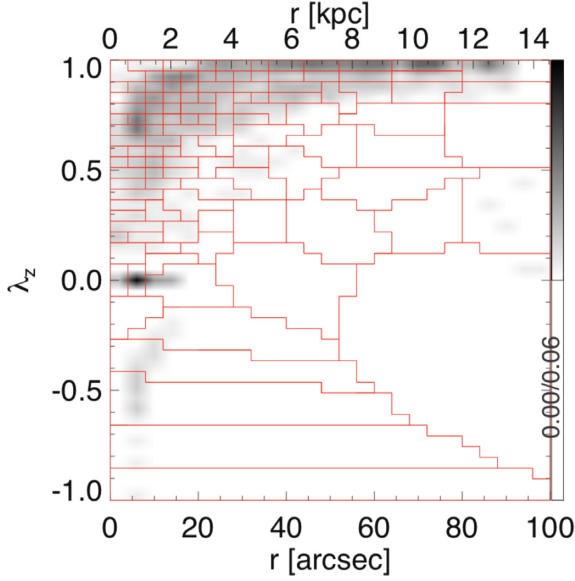


Figure 2. Probability density of stellar orbits in the phase space of circularity λ_z versus time-averaged orbital radius r . Darker colour indicates higher probability as indicated by the colour bar, and the total orbit weight has been normalized to unity. This galaxy has a large fraction of highly circular tube orbits with $\lambda_z \sim 1$ extending to large radius. In the inner regions, there are more tube orbits with significant random motions with $\lambda_z \sim 0.5$, some radial-motion-dominated box orbits $\lambda_z \sim 0$, and a small fraction of counter-rotating (CR) orbits with $\lambda_z < 0$. The red polygons indicate the Voronoi binning scheme we have adopted in the phase space, yielding ~ 100 orbit bundles, each with a minimum weight of 0.005.

N_{bundle} orbital bundles,

$$t_{\text{obs}}^i = \sum_{k=1}^{N_{\text{bundle}}} t_k f_k^i / \sum_k f_k^i, \quad (1)$$

for $i = 1, \dots, N_{\text{obs}}$. Similarly, for metallicity,

$$Z_{\text{obs}}^i = \sum_{k=1}^{N_{\text{bundle}}} Z_k f_k^i / \sum_k f_k^i. \quad (2)$$

We then solve for the values of t_k and Z_k using a Bayesian statistical analysis, which we will describe in detail in Section 3.4. As we will see, reproducing on-sky age and metallicity maps may be possible, however, to reproduce them with the correctly correlated combinations of age and especially metallicity is non-trivial.

3.3 Age–metallicity correlation

We wish to adopt the most agnostic parametrization of the possible metallicity and age values for each orbit bundle. Unfortunately, a completely unconstrained age–metallicity parameter space results in poor recovery of the known 2D distribution in age versus metallicity (see Section 4.3).

In order to provide a theoretically motivated link between age and metallicity that is flexible enough and unbiased for our purposes, we leverage the statistical chemical scaling relations presented in Leaman (2012), and model described by Oey (2000). These essentially map a galaxy’s chemical evolution into a parameter space that is (1) self-similar across time and spatial scales for galaxies of different masses, and (2) easily expressed in a robust statistical functional form (binomial).

The shape of galaxy AMRs and metallicity distribution functions show mass-dependent behaviours (e.g. Kirby et al. 2013; Leaman et al. 2013). However, Leaman (2012) identified that in linear metal fraction (Z/Z_{\odot}), all Local Group galaxies (in mass range

of $M_* < 10^{10} M_{\odot}$) exhibit metallicity distribution functions that are binomial in statistical form, i.e. the variance $\sigma(Z)^2$ and mean $\langle Z \rangle$ are tightly correlated, but the ratio is less than unity. Using a binomial chemical evolution model from Oey (2000), Leaman (2012) demonstrated that galaxies approximately evolve along the $\sigma(Z)^2$ – Z scaling relation. This provides a mass-independent, self-similar framework to link two quantities of interest: the spread in metals and the average metallicity of a galaxy or region of a galaxy.

To further link age to these two quantities we consider the binomial chemical evolution model of Oey (2000), which produces metallicity distribution functions with variance and mean:

$$\begin{aligned} \sigma(Z)^2 &= nQ(1-Q), \\ \langle Z \rangle &= nQ, \end{aligned} \quad (3)$$

where n represents the final number of star-forming generations, and Q represents the covering fraction of enrichment events within a generation. To make time explicit in the model, we consider that the gas reduction increment in the Oey (2000) model, $D = 1 - n\delta$, can be related through the gas fraction definition as

$$\frac{M_{\text{gas}}}{M_*} = \frac{1 - n\delta}{n\delta}. \quad (4)$$

From this we can express an approximate star formation law and relate it to n in the binomial model as

$$n = \frac{M_*}{\delta} = \frac{\int_t^{t_H} \epsilon \text{SFR}(\tau) d\tau}{\text{SFR}(t)}, \quad (5)$$

where t_H is the Hubble time and t is when the last generation of star formation happens. Following empirical and theoretical star formation laws, we have introduced ϵ to allow for non-perfect conversion of gas to stars. This variable is often expressed as an inverse of the gas depletion time: $\epsilon = 1/t_{\text{dep}}$.

For a constant star formation rate, n then becomes

$$n = \frac{t_H - t}{t_{\text{dep}}}, \quad (6)$$

where $t_H - t$ is the length of time that all generations of star formation last in the galaxy. Combining this with the expressions for variance and mean Z in equation (3) we find

$$\sigma(Z)^2 = Z \left(1 - \frac{Z t_{\text{dep}}}{t_H - t} \right). \quad (7)$$

This can then be re-expressed as a link between age, average metallicity, and spread in metallicity:

$$t = t_H - t_{\text{dep}} \frac{Z}{1 - \sigma(Z)^2/Z}. \quad (8)$$

We can now use equation (8) to set a mass-independent link between age and metallicity distributions. To further link these quantities and specify the metallicity spread in terms of average metallicity, we consider the observed statistical correlations present in metallicity distributions of Local Group dwarf to MW-mass galaxies. Empirically, the observed relation between $\sigma(Z)$ and Z from Local Group galaxies (Leaman 2012):

$$\sigma(Z)^2 = 10^{a+b \log 10(Z)}, \quad (9)$$

where $a = -0.689$ and $b = 1.889$ shown as the black solid line in the top panel of Fig. 3. As our priors are best expressed in natural log space, and considering $\ln Z$ of each population follows a Gaussian distribution, then a purely mathematical calculation yields

$$g(Z) \equiv \sigma(\ln(Z)) = \sqrt{\ln(1 + \sigma(Z)^2/Z^2)}. \quad (10)$$

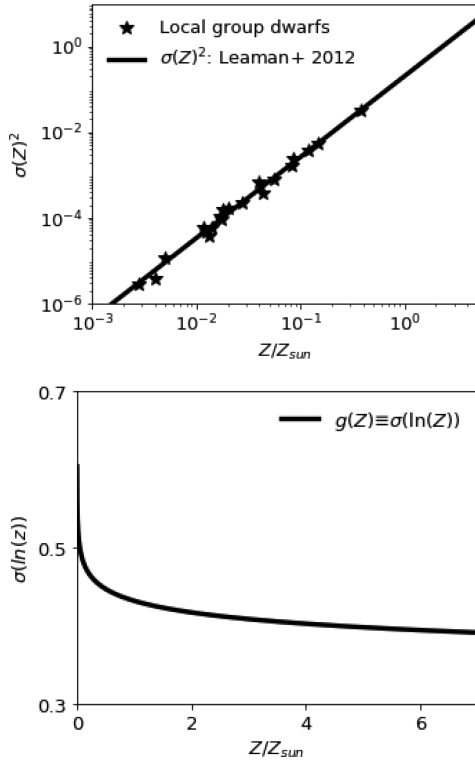


Figure 3. Top: the relation of metallicity spread $\sigma(Z)$ versus Z , the black stars are Local Group dwarf galaxies from Leaman (2012), the black curve (labelled as a) is fitting to these data points (equation 9). Bottom: $\sigma(\ln(z))$ versus Z converted from the curve in the top panel based on equation (10).

Combined with equation (9), this yields for $g(Z)$, the black solid curve shown in the bottom panel of Fig. 3.

Setting $t_H = 14$ Gyr and by substituting $\sigma(Z)^2$ from equation (9) into equation (8), we obtain a relation between average metallicity Z and formation time t . This AMR $Z(t|t_{\text{dep}})$ still depends on depletion time t_{dep} . As shown in Fig. 4, $Z(t)$ is steeper with smaller t_{dep} , and shallower with larger t_{dep} . Actually, t_{dep} will likely be different for different regions in a galaxy with complicated SFH. The dots overplotted in Fig. 4 are the observed age t_{obs} and metallicity Z_{obs} (Au-6 $\theta = 80^\circ$) coloured by their elliptical radius $R_{\text{ellip}} = \sqrt{x^2 + y^2}/(q_{\text{obs}})^2$ on the observational plane, where q_{obs} is observed flattening of the galaxy. There is almost a linear correlation between t_{dep} indicated by $(t_{\text{obs}}, Z_{\text{obs}})$ and radius R_{ellip} (also see Fig. A1 in Appendix A). The star formation in a galaxy is consistent with smaller t_{dep} at small radii, and larger t_{dep} at large radii. We note that the range of depletion times is consistent with those found for a wide range of galaxy masses, regions – including at larger redshifts (cf. Bigiel et al. 2011).

3.4 Bayesian analysis

We use Bayesian statistical analysis (PYTHON package PYMC3) to obtain age (t_k) and metallicity (Z_k) of the orbital bundles.

3.4.1 Fit to age map

We first fit the age map following equation (1). To use Bayesian theorem to compute the posterior $p(\theta|x)$ of a model, we require the prior $p(\theta)$ and the data likelihood $p(x|\theta)$. We adopt a bounded

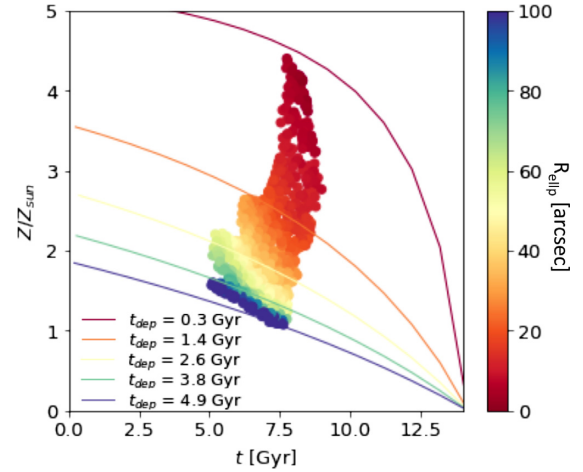


Figure 4. The age–metallicity relation (AMR) $Z(t|t_{\text{dep}})$ derived with combination of equations (8) and (9). The solid curves with different colours are $Z(t)$ by choosing different t_{dep} as labelled. The dots are the observed age t_{obs} and metallicity Z_{obs} (Au-6 $\theta = 80^\circ$) coloured by their elliptical radius R_{ellip} on the observational plane.

normal distribution for the prior of t_k ,

$$f(t_k|\mu_k, \sigma_k) = \sqrt{\frac{1}{2\pi\sigma_k^2}} \exp\left(-\frac{(t_k - \mu_k)^2}{2\sigma_k^2}\right), \quad (11)$$

with lower and upper boundary of 0 and 14 Gyr, we set μ_k and σ_k as follows:

$$\mu_k = \text{Randn}(< t_{\text{obs}} >, 2\sigma(t_{\text{obs}})), \quad (12)$$

$$\sigma_k = 2\sigma(t_{\text{obs}}), \quad (13)$$

where $< t_{\text{obs}} >$ and $\sigma(t_{\text{obs}})$ indicate average and standard deviation of age from the observational age map. Note that $\text{Randn}(a, b)$ means a random number generated from normal distribution with centre a and dispersion b , the above priors are uniform for all the orbital bundles.

Next, we require the data likelihood $p(x|\theta)$ (or called ‘observed stochastic’). Even though the observed data are known and fixed, we need to formally assign it a probability distribution as if it were a random variable. We adopt a student’s t -distribution $t_\nu(x|\mu(\theta), \sigma)$ for the data likelihood (Salvatier, Wiecki & Fonnesbeck 2016). It will allow some outliers in the data and results in a robust fitting. The chain is initialized with the method automatic differentiation variational inference (ADVI) with 200 000 draws, and we run 2000 steps. We take the average and standard deviation of the last 500 steps of the posterior chain as mean and 1σ uncertainties of t_k . The last 500 steps will also be used for smoothing the overall age distribution of the galaxy obtained by our model.

In general, we expect stellar kinematics to be systematically correlated with stellar age, because stars on dynamical hot orbits are systematically older than stars on near-circular orbits (Trayford et al. 2019). From our experience, with the above priors for t_k , it is not easy to perfectly recover the correlation between stellar age t and orbits’ circularity λ_z , especially for the face-on galaxies (see Section 4.4). The results could be improved by fitting a linear relation $t = t_0 + p\lambda_z$ ($\lambda_z \geq 0.0$) to the $t(\lambda_z)$ relation of the first

model.¹ Then for the second model iteration, we set the μ_k and σ_k of the Gaussian priors as

$$\begin{aligned} \mu_k &= \text{Randn}(t_0 + p\lambda_{z,k}, 2\sigma(t_{\text{obs}}) - |p|/2) \quad (\lambda_{z,k} \geq 0.0) \\ &= t_0 \quad (\lambda_{z,k} < 0.0), \end{aligned} \quad (14)$$

$$\sigma_k = 2\sigma(t_{\text{obs}}). \quad (15)$$

In this case, the standard deviation of μ_k s is still $\sim 2\sigma(t_{\text{obs}})$, similar to the previous prior. We perform the Bayesian analysis again with the new priors. This iterative process could be repeated more than once, but we found the results already converged after the first iteration. We stress this is only an iterative refinement on the choices of priors, not a prescribed link between age and circularity directly.

3.4.2 Fit to metallicity map

After we have obtained ages of the orbital bundles, we then fit the metallicity map following equation (2). Metallicity expressed in linear unit Z/Z_\odot is adopted in our analysis. We use a bounded lognormal distribution as prior of metallicity Z_k of each orbital bundle,

$$f(Z_k|\mu_k, \sigma_k) = \frac{1}{Z_k} \sqrt{\frac{1}{2\pi\sigma_k^2}} \exp - \frac{(\ln Z_k - \mu_k)^2}{2\sigma_k^2}, \quad (16)$$

with lower and upper boundary of 0 and 10. We first start with μ_k and σ_k of the lognormal distribution as follows:

$$\mu_k = \ln(\text{Randn}(<Z_{\text{obs}}>, \sigma(Z_{\text{obs}}))), \quad (17)$$

$$\sigma_k = \sigma(Z_{\text{obs}}), \quad (18)$$

where $<Z_{\text{obs}}>$ and $\sigma(Z_{\text{obs}})$ are the average value and standard deviation of metallicity from the observational metallicity map. Then we perform Bayesian analysis similar to the fitting of age map. We take the average and standard deviation of the last 500 steps of the Markov chain Monte Carlo (MCMC) as mean and 1σ error of $\ln(Z_k)$, the last 500 steps are also used for smoothing the overall metallicity distribution of the galaxy obtained by our model.

The above uniform priors for Z_k lead to a poor recovery of the age–metallicity distribution. To this end, we use the AMR derived in Section 3.3 to give more reasonable priors for Z_k , with age of each orbit t_k already obtained. We adopt again the bounded lognormal distribution, but now with μ_k and σ_k given by

$$\mu_k = \ln(Z(t_k|t_{\text{dep}}(r_k))), \quad (19)$$

$$\sigma_k = g(\mu_k). \quad (20)$$

We let the depletion time locally vary as a function of radius r_k (which traces mass density), and refer the reader to Appendix A for details.

In order to understand how the different priors on t_k and Z_k affect our results, we perform two model fits to age and metallicity maps: an unconstrained version, and one with the above-mentioned priors. These are summarized in Table 2. The model results from these different priors are marked as R1 and R2, respectively, throughout the paper.

¹For the spiral galaxies that we test, our model has relatively large uncertainty on stellar ages of the small fraction CR orbits with $\lambda_z < 0.0$, thus we do not include them for the t – λ_z fit.

Table 2. The priors for the Bayesian fitting to age and metallicity maps. We have ~ 100 orbital bundles in the model, k indicates any of these. We take a bounded normal distribution as prior for t_k (equation 11), a bounded lognormal distribution for Z_k (equation 16), with the mean μ_k and dispersion σ_k specified differently for the two rounds of model fitting: R1, R2. When fitting to age, for model R1, we use uniform priors for t_k , and for model R2 we use a relation $t_k = t_0 + p\lambda_{z,k}$ fitted from the result of model R1. When fitting to metallicity, for model R1 we use uniform priors for Z_k , while for model R2 we use the age–metallicity spread relation $Z(t|t_{\text{dep}})$ (Fig. 4), $g(Z)$ (Fig. 3) (see Section 3.3).

Model	Prior for age t_k Norm($t_k \mu_k, \sigma_k$)
R1	$\mu_k = \text{Randn}(<t_{\text{obs}}>, 2\sigma(t_{\text{obs}}))$ $\sigma_k = 2\sigma(t_{\text{obs}})$
R2	$\mu_k = \text{Randn}(t_0 + p\lambda_{z,k}, 2\sigma(t_{\text{obs}}) - p /2)$ $\sigma_k = 2\sigma(t_{\text{obs}})$
Model	Prior for metallicity Z_k LogNorm($Z_k \mu_k, \sigma_k$)
R1	$\mu_k = \ln(\text{Randn}(<Z_{\text{obs}}>, \sigma(Z_{\text{obs}})))$ $\sigma_k = \sigma(Z_{\text{obs}})$
R2	$\mu_k = \ln(Z(t_k t_{\text{dep}}(r_k)))$ $\sigma_k = g(\mu_k)$

4 RESULTS ON STELLAR ORBIT AND POPULATION DISTRIBUTIONS

In this section, we describe how the models match the intrinsic orbit distribution, age–metallicity distribution, and age–circularity correlation with the nine MUSE-like mock data created from Auriga simulation. For illustration of model fitting and some results, we do not show all nine galaxies but just Au-6 $\vartheta = 80^\circ$. We refer the reader to Appendix B for results for the other galaxies.

4.1 Best-fitting model

A best-fitting model of the mock data from Au-6 with $\vartheta = 80^\circ$ is shown in Fig. 5. From left to right, the columns are surface mass density, mean velocity, velocity dispersion, h_3 , h_4 , age (t), and metallicity (Z). The first row is the data, the second row is reproduced by the best-fitting model, and the third row is residual. The model matches the kinematic maps, age and metallicity maps well. For just the projected on-sky maps, we see that the models with different priors (R1, R2) fit the age and metallicity maps equally well.

In summary, up to this point we have obtained an orbit–superposition model, with the orbit weights solved by matching the stellar mass distribution and kinematic maps. Here we further divided the orbits into ~ 100 bundles, and obtained the age and metallicity of these bundles by fitting the age and metallicity maps. By taking a Bayesian statistical analysis, we obtained the mean value t_k and Z_k of each bundle k , as well as their uncertainties $\sigma(t_k)$ and $\sigma(Z_k)$.

4.2 Stellar orbit distribution

We first check how well the orbit distribution in our model matches the true distribution from the simulation. The real gravitational potential and 6D phase-space information of particles are known in the simulation. Thus we know the instantaneous circularity λ_z

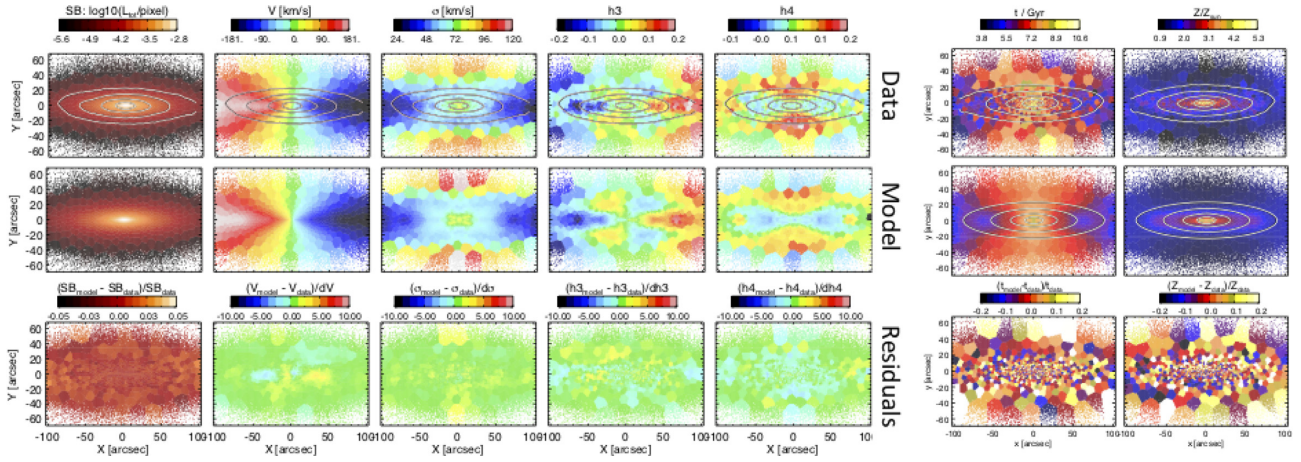


Figure 5. The best-fitting model. The columns are surface mass density, velocity V , velocity dispersion σ , GH coefficient h_3 , h_4 , age t , and metallicity Z . The first row is observational data, the second row is from the best-fitting model, and the third row is residuals.

of each particle (Gómez et al. 2017), which does not necessarily conserve λ_z when orbiting in the potential, especially for those particles on radial/box orbits with $\lambda_z \sim 0$. To obtain the orbits' circularity, in principle, we have to freeze the potential, integrate the particle orbits in the potential, and calculate the average values along the orbits. Here for simplicity, we use a single snapshot and select those particles that are close in energy, E , angular momentum, L_z , and the total angular momentum amplitude, $|L|$. Under the assumption that these particles are on the same orbit in a near-axisymmetric system, we then compute the corresponding averages of radius r and circularity λ_z of these particles, which are taken as the orbit's r and λ_z . The stellar orbit distribution of one galaxy is then presented as the probability density distribution of all these orbits in the phase space of r versus λ_z , which is shown in the left-hand panel of Fig. 6 for Au-6.

In our model, we calculate orbit's circularity and time-averaged radius from the particles sampled from the orbit with equal time interval. The middle panel of Fig. 6 shows the distribution of orbits in our best-fitting model for mock data Au-6 $\vartheta = 80^\circ$.

Our model matches the major features in the phase space of r versus λ_z as the true orbit distribution from the simulations. For the case of Au-6 $\vartheta = 80^\circ$ we show here counter-rotating (CR) orbits contribute a small fraction in the simulation, and our model underestimates CR orbits by ~ 50 per cent. The right-hand subpanel is the marginalized λ_z distribution. The black dashed curve is the true distributions; red solid curve represents that from our model. We did a 1D Kolmogorov–Smirnov (KS) test to check how well the λ_z distribution recovered by our model match the true distribution from simulation. The D-statistics, D , is the maximum deviation from the accumulated curves of two distributions. We obtained $D = 0.09$ here for the λ_z distribution. A similar comparison for Au-5, Au-6, and Au-23 with inclination angles of $\vartheta = 40^\circ$, 60° , and 80° is shown in Appendix B (Fig. B1).

4.3 Age-metallicity distribution

Age and metallicity maps projected on-sky can be reproduced with many degenerate combinations of age-metallicity distributions of the stars. However, not all combinations may be physical, nor match the intrinsic age versus metallicity distribution of the simulated galaxy. Here we check how the age and metallicity distribution of

orbits in our models match the intrinsic distribution of particles in these simulations.

In Fig. 7, we show the probability density distribution of particles/orbits in age (t) versus metallicity (Z/Z_\odot), from the simulations and from our model of Au-6 $\vartheta = 80^\circ$. The first panel labelled with ‘True’ shows the true distribution in age versus Z of particles in the simulation. The following panels are those obtained by our model for mock data $\vartheta = 80^\circ$ but with prior R1, R2 from left to right. The probability contours are smoothed by the last 500 steps of MCMC chains of t_k and Z_k from the Bayesian analysis.

The upper subpanel for each halo is the marginalized age distribution and the right-hand subpanel is the marginalized metallicity distribution. The black dashed curve is the true distributions; red and blue solid curves represent those from models with prior R1 and R2, respectively. From a 1D KS test, we obtained $D = 0.12$ and 0.08 for age distribution and $D = 0.12$ and 0.06 for metallicity distribution, for models with prior R1 and R2, respectively. Both intrinsic age and metallicity distributions are recovered better with model R2 than R1.

In the true distribution, most stars follow a relation with older stars that are more metal poor. Model R1 hardly recovers this relation (Fig. 7), missing a significant fraction in mass of subsolar metallicity stars, and showing roughly uncorrelated distributions of constant metallicity groupings over a wide range in age. The recovery of AMR significantly improved with model R2, especially for more face-on galaxies (see Figs B2 and B3).

4.4 Age-circularity correlation

In this section, we study the correlation of stellar orbit circularity and ages in the simulation, and check how well the correlation can be recovered by our models.

The intrinsic probability density distribution of orbits on age t versus circularity λ_z for simulation Au-6 is shown in the left-hand panel of Fig. 8. Darker colour indicates higher probability density. In the simulation, there is a correlation between stellar age and orbits' circularity: highly circular orbits are systematically younger, and radial-motion-dominated orbits are older. We calculate the average age of orbits as a function of λ_z by binning on λ_z (the magenta dashed curve) and average λ_z as a function of age by binning on age t (the green dashed curve).

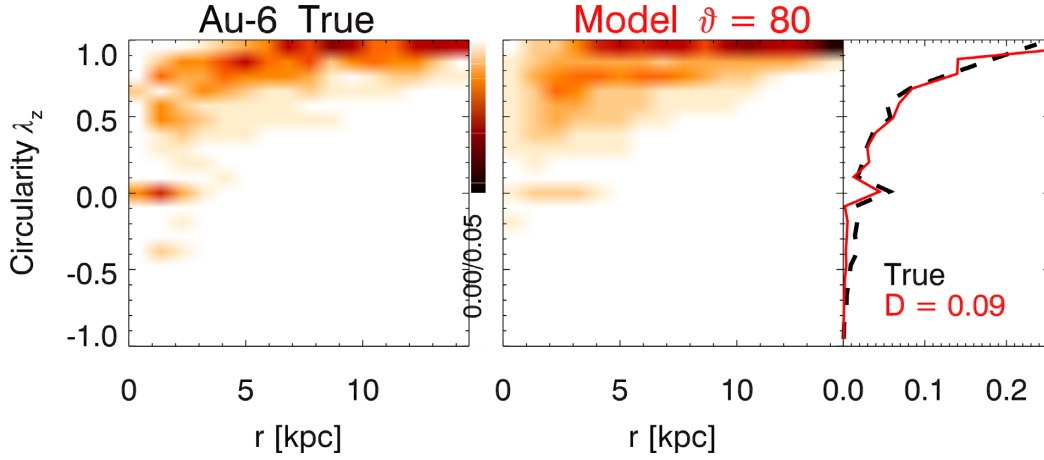


Figure 6. The stellar orbit distribution described as probability density of orbits in the phase space of λ_z versus r , for Au-6. The left-hand panel is the true stellar orbit distributions from simulations. The second is the distribution of orbits in our best-fitting model for mock data with $\theta = 80^\circ$. The right-hand panel is comparison of marginalized λ_z distribution between true and model. Similar figures for the other galaxies are included in Appendix B (Fig. B1).

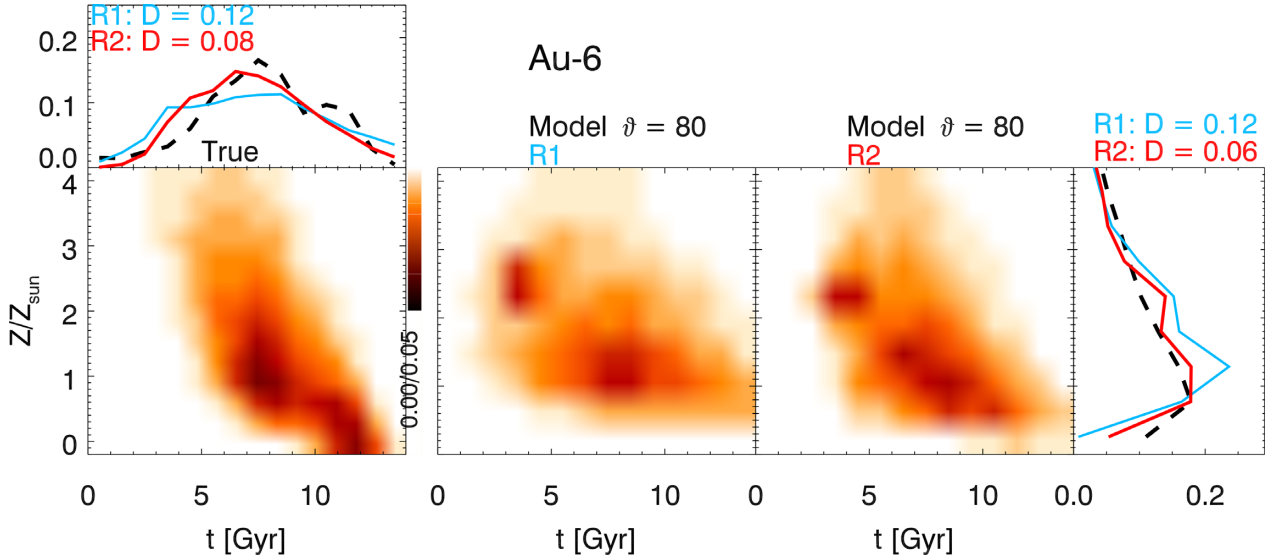


Figure 7. The intrinsic age–metallicity distribution for Au-6 $\theta = 80^\circ$. The left-hand panel is the true distribution in stellar age t versus metallicity Z of particles of the simulation. The rest panels are obtained by our model constrained by mock data Au-6 $\theta = 80^\circ$ with priors R1 and R2 from left to right. The probability contours of our models are smoothed by the last 500 steps of MCMC chains of t_k and Z_k from the Bayesian analysis. The upper subpanel is the marginalized age distribution and the right-hand subpanel is the marginalized metallicity distribution. The black dashed curve is the true; red and blue solid curves represent that from model with priors R1 and R2, respectively. The D-statistics, D , calculated from KS test comparing 1D age/metallicity distribution from our model to the true age/metallicity distribution is labelled.

The orbit distribution in age versus circularity obtained by our models with Au-6 $\theta = 80^\circ$ is shown in the following panels, for model R1 and R2, respectively. In each panel, the probability contours represent the distribution that is derived from the last 500 steps of MCMC chain of t_k from the Bayesian analysis. The magenta triangles are average age as function of λ_z from the model. The magenta solid line ($t = t_0 + p\lambda_z$) is a linear fit to the triangles, which from model R1 is used as prior of age t_k for model R2 when fitting to age map. The green diamonds are average λ_z as a function of age by binning from age from the model.

Our models generally match the t – λ_z correlation from the simulation, model R2 matches it better than R1 for Au-6 $\theta = 80^\circ$; the improvement of R2 comparing to R1 is more significant for more face-on galaxies (see Figs B4 and B5). The results in following sections are based on model R2 if not otherwise specified.

5 ORBITAL DECOMPOSITION

To further quantify the correlation between the orbits' dynamical properties and stellar populations, we decompose galaxies (cf. Zhu et al. 2018b) by dividing the orbits into cold ($\lambda_z \geq 0.8$), warm ($0.25 \leq \lambda_z < 0.8$), hot ($|\lambda_z| < 0.25$), and CR ($\lambda_z < -0.25$) components. We emphasize that the separation of cold, warm, hot+CR components is just for proof of concept. For real galaxies, we may adjust the component separation case by case.

We rebuild the 3D structure for each of the cold, warm, hot+CR components by particles in simulations and orbits in models. Then we project the 3D structures, here with the same inclination angle as the galaxy was observed, to the observational plane, thus obtaining surface density (SD), velocity and velocity dispersion, and age and metallicity maps for each component. In Fig. 9, we compare these

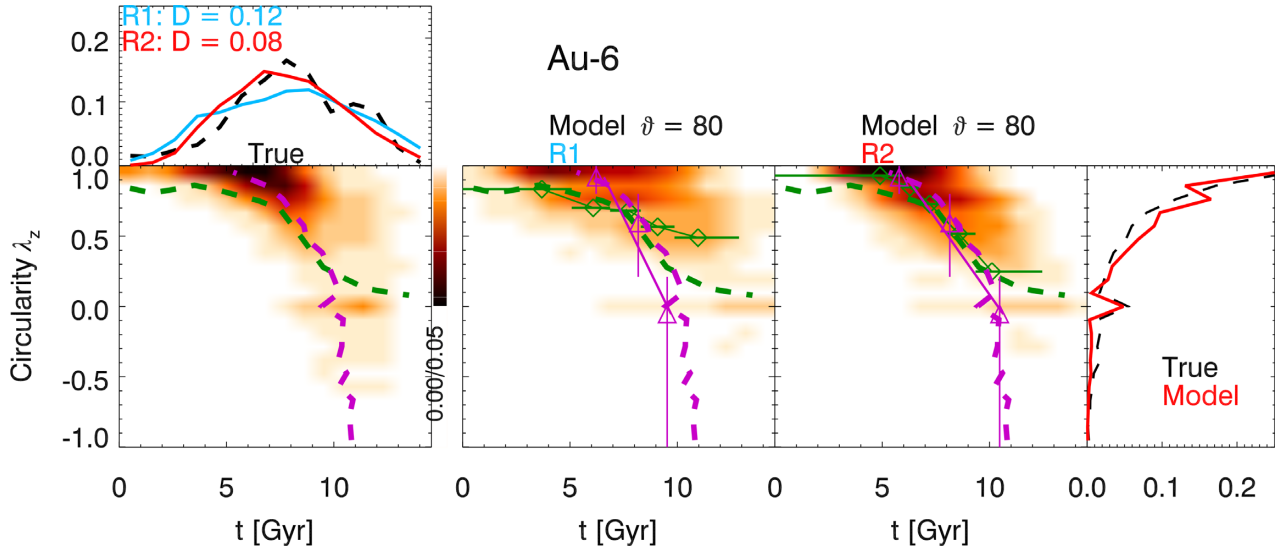


Figure 8. The intrinsic correlation of age versus circularity, for Au-6 and those from our models with mock data $\vartheta = 80^\circ$. The first one is the true distributions of the particles from simulation, darker colour indicates higher probability density, the magenta dashed curve is average age t as a function of λ_z , while the green dashed curve is average λ_z as a function of age t from the simulation. The following panels are obtained by model R1 and R2, respectively. In each panel, the magenta triangles are average age as a function of λ_z for the corresponding panel, the magenta solid line is a linear fit ($t = t_0 + p\lambda_z$) to the triangles. The magenta solid line from model R1 is used as priors of ages t_k in model R2. Similarly, the green diamonds represent average λ_z as a function of age t for the model. Model R2 matches the true relations in the simulation better than model R1.

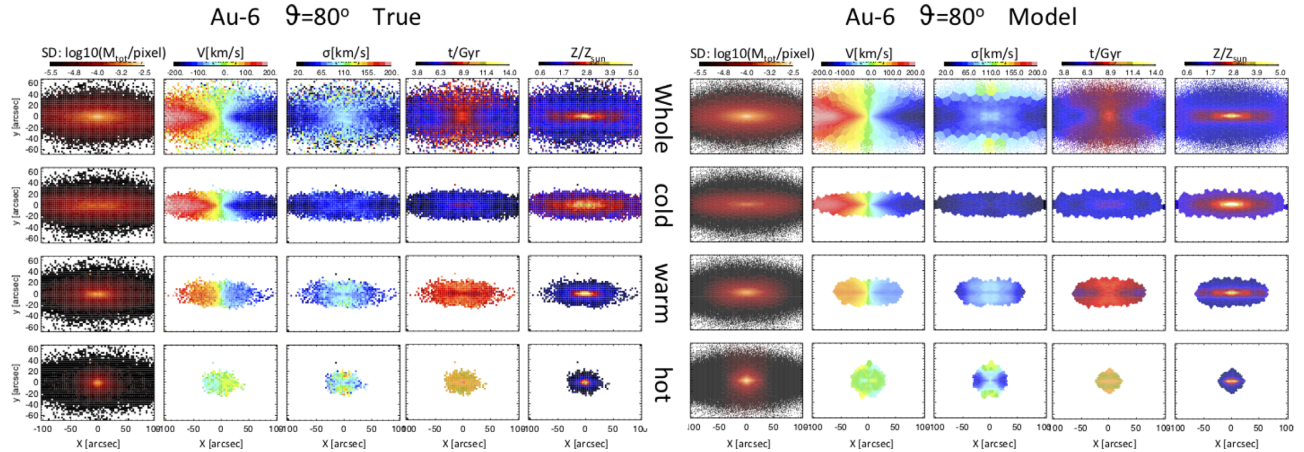


Figure 9. Surface mass density and age and metallicity maps of the whole galaxy, cold, warm, and hot+CR component (from top to bottom) of Au-6 $\vartheta = 80^\circ$. The left-hand panels are constructed by particles in the simulation, the right-hand panels are constructed by orbital bundles in our model constrained by mock data with $\vartheta = 80^\circ$. The galaxy is at a distance of 30 Mpc, 1 arcsec = 145 pc.

maps from the simulation Au-6 (left) to those recovered from our model with mock data Au-6 $\vartheta = 80^\circ$ (right).

Our model generally reproduces the morphology, kinematics, and age and metallicity maps of the different components: the cold thin disc is fast rotating with small velocity dispersion, young, and metal rich; the warm thicker component has weaker rotation and higher velocity dispersion, older, and metal poorer; and the hot+CR spheroid has almost no rotation and high velocity dispersion, with oldest and most metal-poor stellar populations. The 2D maps, both along the major and minor axis, of each component are visually well recovered by our model.

For a quantitatively comparison, we show in Fig. 10 the radial profiles (along the major axis) of the SD, age, and metallicity for the cold, warm, and hot+CR component, obtained from the simulation (left) and from our model (right). The three components are plotted

as black, yellow, and red. In the right-hand panels, we show not only the best-fitting model, but also all the models within 1σ uncertainty when fitting to kinematics (Zhu et al. 2018b). The shadow areas indicate the scatter of these models within 1σ uncertainty, the solid thick curves are corresponding averages, and the thin dashed curves are the best-fitting one.

The cold thin disc is spatially extended with a SD profile close to exponential, the warm component is less extended, while the hot+CR spheroid is concentrated in the inner regions. The SD profiles of the three components are generally reproduced well by our model. Note that we slightly overestimate the SD of warm components, although the warm component itself is a small fraction compared to the cold component at the outer regions.

The simulation shows an increase in stellar age from cold to hot orbits, with little change in that behaviour with galactocentric

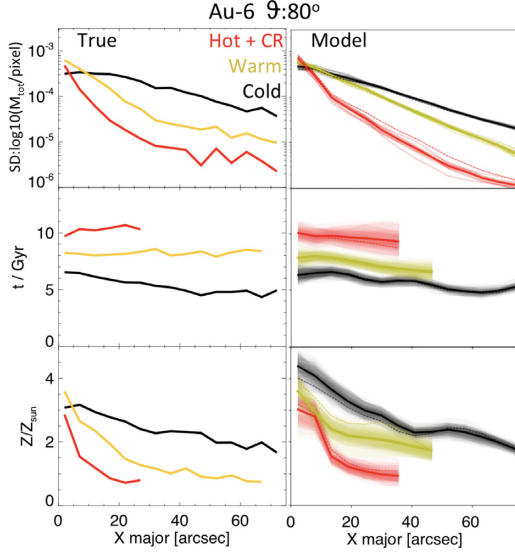


Figure 10. Surface mass density, age, and metallicity profiles along major axis (1 arcsec = 145 pc) of the cold (black), warm (warm), and hot+CR (red) component of Au-6 $\vartheta = 80^\circ$. The left-hand panels are constructed by particles in the simulation. The right-hand panels are those constructed by orbital bundles in our model constrained by mock data with $\vartheta = 80^\circ$, the shadow regions indicate 1σ uncertainty of our models, the solid thick curves are average of models within 1σ , and the dashed thin curves are the best-fitting one.

distance; there is only a shallow negative gradient for the cold disc from inner to out regions. Our models generally reproduce this behaviour. An implication of this is that for the galaxy as a whole, the projected age gradient is a result of different dynamical components superimposed: the old-hot component dominates in the centre and a young-cold component dominates in the outer regions.

The three components have similar metallicity (Z/Z_\odot) at the centre, with a strong negative metallicity gradient in the hot+CR component, and the gradient becomes weaker from hot+CR, warm to cold component. Our models generally match the metallicity gradients for warm and hot+CR component, but overestimate the metallicity of cold component in the inner region, thus resulting in a too strong metallicity gradient for the cold component.

A similar decomposition is performed for all galaxies. For edge-on galaxies ($\vartheta = 80^\circ$), the age and metallicity profiles of three components are recovered similarly well for Au-5, Au-6, and Au-23 (see Figs B6 and B7). Age and metallicity profiles of each component are recovered less well in more face-on galaxies.

6 GLOBAL AGE-DISPERSION RELATION

The stellar age versus vertical velocity dispersion σ_z relation is widely used for resolved systems to study the dynamical heating processes (e.g. Leaman et al. 2017). Here, we extract similar relations for external galaxies based on our model to galaxies with integrated-light data. Application of a similar approach to NGC 3115 has provided a t - σ_z relation of this galaxy (Poci et al. 2019). Here, we check how reliable the global (not disc alone) t - σ_z relation can be recovered.

We can construct t - σ_z relations by separating the galaxies into multiple components in two ways based on Fig. 8, by applying a cut either on circularity λ_z , or on stellar age of the orbits in our model.

First we follow the separating on circularity λ_z as we did in

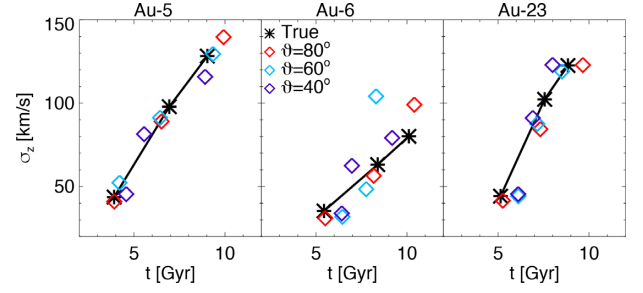


Figure 11. The global age t versus dispersion σ_z relation. The three panels are for Au-5, Au-6, and Au-23, respectively. We separate each galaxy to be cold, warm, hot+CR components based on the orbits' circularity λ_z , and calculate average age and dispersion σ_z for each component. In each panel, the black asterisks are the true values calculated from the simulations, dispersion increases with age from cold, warm to hot component, the solid black curve just connects the asterisks. The red, blue, and purple diamonds represent those calculated from our models for galaxies with $\vartheta = 80^\circ$, 60° , and 40° , respectively.

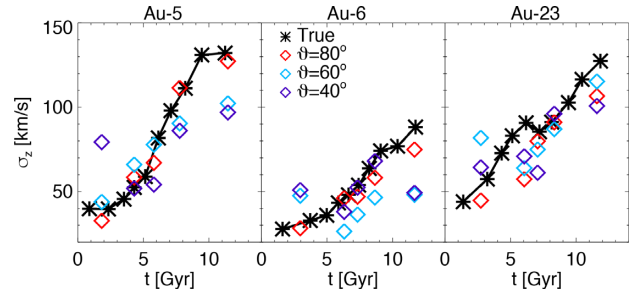


Figure 12. The global age t versus dispersion σ_z relation. Similar to Fig. 11, but by separating the simulation/model into equal mass bins according to stellar age. We separate the simulation into 10 age bins, and model into five age bins.

last section, to separate the simulation/model into cold, warm, hot+CR components, then we calculate the average age and σ_z of each component. In Fig. 11, we show the resulting t - σ_z relation in these simulations and how our model recovered it. The three panels are for Au-5, Au-6, and Au-23, respectively. In each panel, the black asterisks are the true ages and velocity dispersions σ_z of each component from the simulation. There are strong age versus σ_z correlation in these three Auriga simulations; cold components have small σ_z and are younger, while hot components have larger σ_z and are older.

The red, blue, and purple diamonds represent those calculated from our models for galaxies with $\vartheta = 80^\circ$, 60° , and 40° , respectively. For all three simulations, our models match the average age of each orbital component well, thus also the t - σ_z correlation. There are slightly larger offsets for the face-on galaxies ($\vartheta = 40^\circ$), but they still generally match the trend. Our method works better for Au-5 and Au-23, in which the intrinsic age- σ_z correlations are steeper, than Au-6, in which the correlation is shallower.

As local observations have traditionally computed the velocity dispersion of stars in similar age bins, we also separate the galaxy by applying cuts on stellar age, with equal mass in each bin. We use 10 age bins for the simulation, and five age bins for the models, and calculate average age and dispersion in each bin. In this way, it can be compared to similar observed vertical dispersion of galaxies at high redshift. The resulting t - σ_z relation is shown in Fig. 12.

By binning along stellar age, our models still recover the t - σ_z relation reasonably well for edge-on galaxies. It is recovered

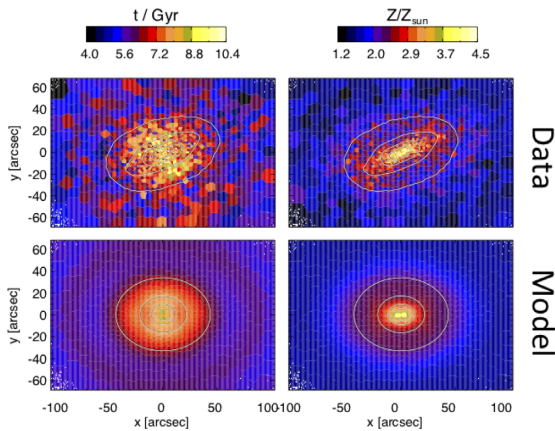


Figure 13. The best-fitting model of age (left) and metallicity (right) maps of Au-23 $\vartheta = 40^\circ$. The first row is the mock data, a bar-like structure is not obvious in age map, but significant in metallicity, the contours overlapped illustrate the real surface mass density of the galaxy that has a strong barred structure. The second row is our model fitted age and metallicity maps, the overlapped contours illustrate the surface mass density of our model.

less well for face-on galaxies, for which σ_z of old populations are underestimated by our model. This is likely due to the relative large uncertainty of age of each orbital bundle. Some cold orbits could get old ages, and so contaminate the old populations and lead to an underestimation of σ_z .

7 DISCUSSION

We have shown that our population-orbit superposition methods work well in recovering the intrinsic stellar orbit distributions and stellar population distributions of external galaxies. This method could be widely applied to nearby galaxies with IFU observations, making it possible to separate structures in external galaxies from a combination of stellar kinematics and stellar chemical properties, thus bridging the gap between the MW and external galaxies.

The current method works well in a few important aspects, but also as we have shown, the interpretation of some results need to be taken with caution as it does not work equally well for all projections. Here we discuss in detail some limitations and how to improve it in the future.

7.1 Features of bars

We do not have a bar structure explicitly in the model, while Auriga galaxies are strongly barred. The bar regions of these galaxies are filled by mostly warm orbits with similar circularity in our model as the resonant orbits supporting the real bar in the simulation. Bars generally have stellar age slightly younger than the discs, but are significantly metal richer, consistent with the observational results (Neumann et al. 2020). We take Au-23 $\vartheta = 40^\circ$ shown in Fig. 13 as an example. The first row shows the mock data of age and metallicity maps with contours showing the real surface mass density. The second row is our best fit to the data with contours showing surface mass density in our model. The bar is not a prominent feature in the age map, but much more obvious in the metallicity map. Based on the orbital constructions in our model, we do not have the ability to match the bar structure in the metallicity map. This could directly lead to a bias in the recovered metallicity for different orbital components.

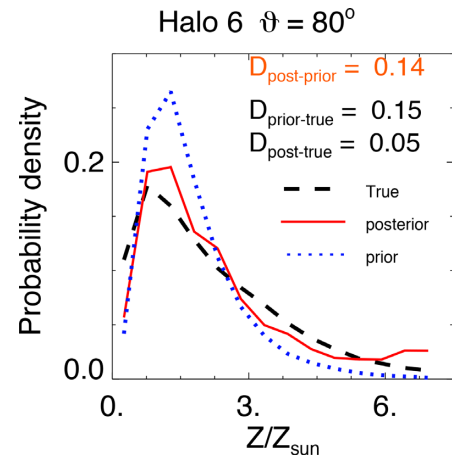


Figure 14. Difference between prior and posterior distributions of metallicity for halo 6 $\vartheta = 80^\circ$. The black dashed curve is the real metallicity distribution in the simulation, the blue dotted curve is the prior distribution set by the age–metallicity relation (AMR), and the red solid curve is the posterior distribution after fitting to the data. We use D-statistics to quantify the difference of two distributions, the D value between any of the two distributions is labelled.

For edge-on cases, the structure in metallicity caused by the bar could be roughly matched by assigning different metallicities to the corresponding warm orbits, thus our model can still work on recovering metallicities of cold, warm, hot+CR components. This is not the case for face-on projections. Including a bar explicitly in our Schwarzschild model in the future, as attempted in other studies (Vasiliev & Valluri 2020), will certainly lead to improving recovery of metallicities of different structures in barred galaxies.

In the current model, we group the orbits into bundles on a 2D phase space of radius r versus circularity λ_z , but do not include (a proxy for) a third integral of motion. With this grouping, the age and metallicity maps are already fitted remarkable well, except for the bar regions. In order to fit the bar in age and metallicity, orbit bundles divided on a 3D phase space rather than 2D might be needed to fit the corresponding features.

7.2 Priors

An iterative fitting procedure is used for age, starting with uninformative uniform priors. The correlation between age and circularity from the first step is then used as prior for a second step, etc. Typically only two steps are required to converge to a final age versus circularity correlation. In this way, the resulting age distribution is driven by the data.

Next for metallicity, we use a physically motivated age–metallicity correlation to sample the priors. In Fig. 14, we show the difference between prior and posterior of the metallicity distribution for halo 6 $\vartheta = 80^\circ$. The black dashed curve is the real metallicity distribution in the simulation, the blue dotted curve is the prior distribution set by the age–metallicity correlation, and the red solid curve is the posterior distribution after fitting the data. We use D-statistics to quantify the difference of two distributions, with the D value between any of the two distributions as labelled.

We adopt a flexible age–metallicity prior that obeys some inescapable limits, there is a physical, well-motivated reason that the posterior and prior might be similar. However, as shown in Fig. 14, the prior metallicity distribution is actually far away from the true metallicity distribution ($D_{\text{prior-true}} = 0.15$), there is sufficient information in the data to drive the posterior metallicity distribution

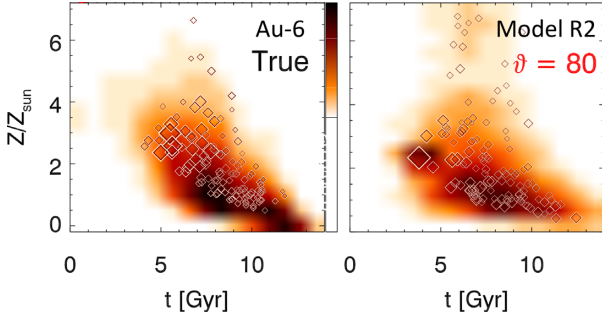


Figure 15. The intrinsic age–metallicity distribution for Au-6 $\vartheta = 80^\circ$. In the left-hand panel, the contours represent the probability density distribution of particles in the simulation, the diamonds represent age versus metallicity of orbital bundles, which we obtained by dividing the particles based on 2D r – λ_z plane. In the right-hand panel, the diamonds are age versus metallicity of orbital bundles in our model, the contours are smoothed by results of the last 500 steps of the PYMC3 process.

very close to the true metallicity distribution ($D_{\text{post-true}} = 0.05$). In the prior distribution, there is low probability (but not zero) to get metallicity Z/Z_\odot higher than 4. While in the observational data, there are some metal-rich points, which drive the posterior distribution to match the true distribution at high Z end. Note that this is still true for face-on galaxies, although in these cases the final distribution matches the real distribution less well but still with $D_{\text{post-true}} < 0.1$ as we show in Fig. B3.

7.3 Beyond single age and metallicity per orbit

We tag a single value of age and metallicity to each orbit bundle divided in the 2D r – λ_z plane, while each orbit bundle should have a distribution of age and metallicities. A consequence of this is the most-poor end of the metallicity distribution is difficult to match completely (see Figs 7 and B3). This can be due to two effects that we explain below.

In the left-hand panel of Fig. 15, the contours are probability density distribution in age versus metallicity of particles in the simulation. We divide the particles into different orbital bundles on r – λ_z , each diamond represents average age and metallicity of an orbit bundle. As can be seen, the age and metallicity distributions of the orbit bundles are narrower than those of true distribution of particles. There are rarely orbit bundles with average $Z/Z_\odot < 0.5$ – even in the simulation. Thus it is expected that when assigning a single value of age and metallicity to each orbital bundle, our model will also show a narrow distribution in age and metallicity (even smoothing over the last samples of our PYMC3 process).

A second related aspect is that our model is reproducing on-sky projected age and metallicity maps. For any projection, even at the high spatial resolution of modern MUSE observations, such spatial binning results in a significant loss in information when compared to the true particle age and metallicities. Further work looking at optimal reconstruction of true particle distributions from binned maps and observational estimates of line-of-sight metallicity and age distributions per pixel will provide help in this front. Technically, it is not difficult to impose an age and metallicity distribution to each orbital bundle. However, the distribution is fully unconstrained by our current data, which are only light/mass weighted age and metallicity maps averaged along line of sight. If we want to constrain the age and metallicity distributions of each orbital bundle, we will need line-of-sight age and metallicity distribution from observation,

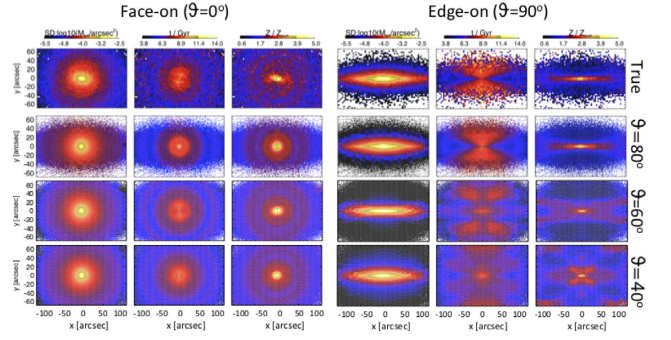


Figure 16. The perfectly face-on (left) and edge-on (right) surface density and age and metallicity maps of halo 6, and those in the models constrained by data halo 6 $\vartheta = 80^\circ$, $\vartheta = 60^\circ$, and $\vartheta = 40^\circ$ from top to bottom.

which we still need to further investigate from the observational side.

We find that the method works better for edge-on than face-on galaxies in a few aspects: recovering the general age versus circularity correlation, the detailed age and metallicity profiles of different dynamical components, and the t – σ_z relation. Apart from the presence of bars, age and metallicity information of different structures, e.g. thin/thick discs and bulge, are revealed in the edge-on age/metallicity maps, while blended in face-on projected data. The ability of recovering 3D age and metallicity structures and other aspects as we mentioned for face-on galaxies could also improve if we can use line-of-sight age/metallicity distribution from observations as model constraints.

7.4 Recovery of 3D distributions

The recovery of a 3D density distribution from a 2D image on the sky-plane is non-trivial even for axisymmetric systems if not edge-on (e.g. Gerhard & Binney 1996). Here by fitting the surface density, kinematics, age, and metallicity maps, we check how the 3D density, age, and metallicity distributions are recovered in our model. In Fig. 16, we show the perfectly face-on ($\vartheta = 0^\circ$) and edge-on ($\vartheta = 90^\circ$) surface density and age and metallicity maps of the simulation halo 6, and those in the models constrained by halo 6 $\vartheta = 80^\circ$, $\vartheta = 60^\circ$, and $\vartheta = 40^\circ$ from top to bottom.

The model constrained by halo 6 $\vartheta = 80^\circ$ matches the face-on and edge-on view of surface density, as well as age and metallicity maps of the true simulation well, except for the central bar regions. While for more face-on galaxies ($\vartheta = 60^\circ$ and $\vartheta = 40^\circ$), the density distributions are more-or-less similar to the true, but the age and metallicity structures at edge-on view are significantly biased. The recovery of 3D density distribution for face-on galaxies benefits from fitting the LOSVD rather than just the zero moments surface density map. Thus the 3D age and metallicity distributions are also expected to be recovered better once we fit the line-of-sight age and metallicity distributions as we discussed in Section 7.3.

8 SUMMARY

We present a population-orbit superposition method in this paper by tagging age and metallicity to orbits in the Schwarzschild model and requiring it to fit the observed luminosity/mass distribution, as well as stellar kinematics and age and metallicity maps. We validate the method by testing against mock data created from simulations. We take three simulations from Auriga, and project each simulation

with three different inclination angles $\theta = 80^\circ$, 60° , and 40° . With each projection, we create a set of mock data with MUSE-like data quality, including surface mass density, stellar kinematics, and age and metallicity maps. Thus, we have nine mock data sets in total, each is taken as an independent observed galaxy, to which we apply our method.

The mock data is fitted well by our model with no difficulty except for the barred features in face-on galaxies. To reproduce correct relations between age and metallicity, we found a physically motivated chemical evolution prescription for the priors significantly improved the results. To evaluate the method's ability of recovering galaxies' intrinsic properties, we compare these properties from our models to those from simulations.

(1) Our models can generally and equally well recover the stellar orbit distribution in the phase space of circularity λ_z versus radius r for galaxies with different viewing angles.

(2) The intrinsic stellar population distribution in age t versus metallicity Z is hard to fully recover. We derived a theoretically motivated link between age, mean metallicity, and metallicity spread, which we impose as priors when fitting metallicity maps. This link improved our recovery of age–metallicity correlations, and the marginalized metallicity distributions.

(3) Our method works well in recovering the age–circularity correlation for edge-on galaxies, but less well for more face-on galaxies. An iterative fitting by updating the priors for age based on an initial fit helps improving the results, especially for face-on galaxies.

(4) To further check the method's ability on recovering intrinsic properties of different galaxy structures, we decompose galaxies into cold ($\lambda_z > 0.8$), warm ($0.25 < \lambda_z < 0.8$), hot+CR ($\lambda_z < 0.25$) components. We then rebuild the surface density, velocity, velocity dispersion, and age and metallicity maps of each component. By comparing with those constructed from the simulation, we find these maps of each component are quantitatively well recovered by our model for projections close to edge-on.

(5) All three simulations have a strong global age(t) versus velocity dispersion (σ_z) correlation such that older stars are hotter with larger σ_z . This relation is well recovered by our method for all galaxies with different projection angles when we bin on circularity: they become older and with larger σ_z from cold, warm to hot components. When we bin on stellar age, the t – σ_z relation is still recovered reasonably well for edge-on galaxies, but we underestimate σ_z of old populations for face-on galaxies.

The results presented will be our basis to apply this method to real data, including case/statistical studies for galaxies with MUSE-like IFU observations. The decomposition of cold, warm, and hot+CR components is not a final solution for dynamical decomposition of real galaxies, as flexible choice for galaxies case-by-case could be investigated. While continued improvements to the methodology will be developed by our team, this proof-of-concept shows great promise in the ability of the method to uncover the build-up and time-scales for formation of different components within galaxies observed with modern IFU instruments.

ACKNOWLEDGEMENTS

It is a pleasure to thank Mariya Lyubenova, Ignacio Martín Navarro, Ortwin Gerhard, Richard Long, and Dandan Xu for stimulating discussions. This research is supported by the National Key Research and Development Program of China under grant no. 2018YFA0404501 (SM, LZ), and National Natural Science Foundation of China under grant no. Y945271001 (LZ). GvdV

and PJ acknowledge funding from the European Research Council (ERC) under the European Union's Horizon 2020 research and innovation programme under grant agreement no. 724857 (Consolidator Grant ArcheoDyn). JF-B acknowledges support through the RAVET project by the grant AYA2016-77237-C3-1-P from the Spanish Ministry of Science, Innovation and Universities (MCIU) and through the IAC project TRACES that is partially supported through the state budget and the regional budget of the Consejería de Economía, Industria, Comercio y Conocimiento of the Canary Islands Autonomous Community. RMM is the recipient of an Australian Research Council Future Fellowship (project number FT150100333).

REFERENCES

- Aumer M., Binney J., Schönrich R., 2016, *MNRAS*, 462, 1697
 Belokurov V., Erkal D., Evans N. W., Koposov S. E., Deason A. J., 2018, *MNRAS*, 478, 611
 Belokurov V., Sanders J. L., Fattahi A., Smith M. C., Deason A. J., Evans N. W., Grand R. J. J., 2020, *MNRAS*, 494, 3880
 Benson A. J., Lacey C. G., Frenk C. S., Baugh C. M., Cole S., 2004, *MNRAS*, 351, 1215
 Bigiel F. et al., 2011, *ApJ*, 730, L13
 Bird J. C., Kazantzidis S., Weinberg D. H., Guedes J., Callegari S., Mayer L., Madau P., 2013, *ApJ*, 773, 43
 Boecker A., Leaman R., van de Ven G., Norris M. A., Mackereth J. T., Crain R. A., 2020, *MNRAS*, 491, 823
 Bundy K. et al., 2015, *ApJ*, 798, 7
 Cappellari M., 2002, *MNRAS*, 333, 400
 Cappellari M., 2017, *MNRAS*, 466, 798
 Carnall A. C., Leja J., Johnson B. D., McLure R. J., Dunlop J. S., Conroy C., 2019, *ApJ*, 873, 44
 Cid Fernandes R., Mateus A., Sodré L., Stasińska G., Gomes J. M., 2005, *MNRAS*, 358, 363
 Cretton N., van den Bosch F. C., 1999, *ApJ*, 514, 704
 Croom S. M. et al., 2012, *MNRAS*, 421, 872
 de Lorenzi F., Debattista V. P., Gerhard O., Sambhus N., 2007, *MNRAS*, 376, 71
 Dutton A. A., Macciò A. V., 2014, *MNRAS*, 441, 3359
 Emsellem E., Monnet G., Bacon R., 1994, *A&A*, 285, 723
 Fattahi A. et al., 2019, *MNRAS*, 484, 4471
 Few C. G., Gibson B. K., Courty S., Michel-Dansac L., Brook C. B., Stinson G. S., 2012, *A&A*, 547, A63
 Gaia Collaboration et al., 2018, *A&A*, 616, A1
 Gebhardt K. et al., 2000, *AJ*, 119, 1157
 Genzel R. et al., 2011, *ApJ*, 733, 101
 Gerhard O. E., 1993, *MNRAS*, 265, 213
 Gerhard O. E., Binney J. J., 1996, *MNRAS*, 279, 993
 Gómez F. A. et al., 2017, *MNRAS*, 472, 3722
 Grand R. J. J., Springel V., Gómez F. A., Marinacci F., Pakmor R., Campbell D. J. R., Jenkins A., 2016, *MNRAS*, 459, 199
 Grand R. J. J. et al., 2017, *MNRAS*, 467, 179
 Grand R. J. J. et al., 2019, *MNRAS*, 490, 4786
 Guérou A., Emsellem E., Krajnović D., McDermid R. M., Contini T., Weilbacher P. M., 2016, *A&A*, 591, A143
 Helmi A., Sales L. V., Starkenburg E., Starkenburg T. K., Vera-Ciro C. A., De Lucia G., Li Y. S., 2012, *ApJ*, 758, L5
 Helmi A., Babusiaux C., Koppelman H. H., Massari D., Veljanoski J., Brown A. G. A., 2018, *Nature*, 563, 85
 House E. L. et al., 2011, *MNRAS*, 415, 2652
 Hunt J. A. S., Kawata D., 2014, *MNRAS*, 443, 2112
 Jenkins A., Binney J., 1990, *MNRAS*, 245, 305
 Jin Y., Zhu L., Long R. J., Mao S., Xu D., Li H., van de Ven G., 2019, *MNRAS*, 486, 4753
 Kirby E. N., Cohen J. G., Guhathakurta P., Cheng L., Bullock J. S., Gallazzi A., 2013, *ApJ*, 779, 102
 Leaman R., 2012, *AJ*, 144, 183

Leaman R., VandenBerg D. A., Mendel J. T., 2013, *MNRAS*, 436, 122
 Leaman R. et al., 2017, *MNRAS*, 472, 1879
 Leja J., Carnall A. C., Johnson B. D., Conroy C., Speagle J. S., 2019, *ApJ*, 876, 3
 Long R. J., 2016, *Res. Astron. Astrophys.*, 16, 189
 Long R. J., Mao S., 2010, *MNRAS*, 405, 301
 Long R. J., Mao S., 2018, *Res. Astron. Astrophys.*, 18, 145
 McDermid R. M. et al., 2015, *MNRAS*, 448, 3484
 Mackereth J. T. et al., 2017, *MNRAS*, 471, 3057
 Marinacci F., Grand R. J. J., Pakmor R., Springel V., Gómez F. A., Frenk C. S., White S. D. M., 2017, *MNRAS*, 466, 3859
 Neumann J. et al., 2020, *A&A*, 637, A56
 Oey M. S., 2000, *ApJ*, 542, L25
 Pakmor R. et al., 2017, *MNRAS*, 469, 3185
 Pinna F. et al., 2019a, *A&A*, 625, A95
 Pinna F. et al., 2019b, *A&A*, 623, A19
 Pizzella A., Morelli L., Coccato L., Corsini E. M., Dalla Bontà E., Fabricius M., Saglia R. P., 2018, *A&A*, 616, A22
 Poci A., McDermid R. M., Zhu L., van de Ven G., 2019, *MNRAS*, 487, 3776
 Portail M., Wegg C., Gerhard O., Ness M., 2017, *MNRAS*, 470, 1233
 Rix H.-W., de Zeeuw P. T., Cretton N., van der Marel R. P., Carollo C. M., 1997, *ApJ*, 488, 702
 Ruiz-Lara T., Few C. G., Gibson B. K., Pérez I., Florido E., Minchev I., Sánchez-Blázquez P., 2016, *A&A*, 586, A112
 Salvatier J., Wiecki T., Fonnesbeck C., 2016, *PeerJ Comput. Sci.*, 2, e55
 Sánchez S. F. et al., 2012, *A&A*, 538, A8
 Sarzi M. et al., 2018, *A&A*, 616, A121
 Springel V., 2010, *MNRAS*, 401, 791
 Stinson G. S. et al., 2013, *MNRAS*, 436, 625
 Tabor M., Merrifield M., Aragón-Salamanca A., Fraser-McKelvie A., Peterken T., Smethurst R., Drory N., Lane R. R., 2019, *MNRAS*, 485, 1546
 Trayford J. W., Frenk C. S., Theuns T., Schaye J., Correa C., 2019, *MNRAS*, 483, 744
 Tsatsi A., Macciò A. V., van de Ven G., Moster B. P., 2015, *ApJ*, 802, L3
 Valluri M., Merritt D., Emsellem E., 2004, *ApJ*, 602, 66
 van den Bosch R. C. E., van de Ven G., Verolme E. K., Cappellari M., de Zeeuw P. T., 2008, *MNRAS*, 385, 647
 van der Marel R. P., Franx M., 1993, *ApJ*, 407, 525
 van der Wel A. et al., 2016, *ApJS*, 223, 29
 van de Ven G., de Zeeuw P. T., van den Bosch R. C. E., 2008, *MNRAS*, 385, 614
 Vasiliev E., Valluri M., 2020, *ApJ*, 889, 39
 Wisnioski E. et al., 2015, *ApJ*, 799, 209
 Zhu L. et al., 2018a, *Nat. Astron.*, 2, 233
 Zhu L. et al., 2018b, *MNRAS*, 473, 3000

APPENDIX A: DEPLETION TIME IN METALLICITY PRIORS

From the observed age (t_{obs}) and metallicity (Z_{obs}) at each position, we can derive a corresponding t_{dep} according to the theoretical relation $Z(t|t_{\text{dep}})$ as shown in Fig. 4. Here in Fig. A1, we show the correlation of t_{dep} with elliptical radius R_{ellip} across the observational plane. t_{dep} is almost linearly correlated with the elliptical radius R_{ellip} . t_{dep} is smaller in the inner regions with large mass density, and larger in the outer regions with small mass density.

The observed metallicity maps have a narrow region of metallicity due to projection effects, compared to the intrinsic metallicity distribution of the particles. Thus the t_{dep} we derived in this way will likely underestimate the true maximum depletion time (and range of depletion times).

As shown in Fig. 4, the observed age and metallicity distributions are bounded by depletion times that correlate with the projected radius of the bins. The upper panels of Fig. A1 show the explicit

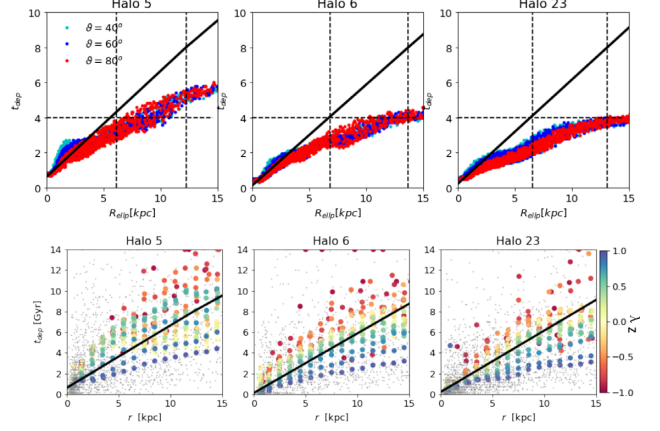


Figure A1. Top panels: correlation of t_{dep} and elliptical radius R_{ellip} for all nine mock galaxies. t_{dep} at each position is derived by $(t_{\text{obs}}, Z_{\text{obs}})$ according to the theoretic relation $Z(t|t_{\text{dep}})$ in Fig. 4. The two vertical dashed lines in each panel indicate R_e and $2R_e$. The thick black lines $t_{\text{dep}}(r) = ar + b$ are determined by two points: $(0, t_{\text{dep, min}})$ and $(R_e, 4 \text{ Gyr})$. Bottom panels: correlation of t_{dep} and intrinsic radius r in the three simulations. The grey dots represent particles in the simulation, the coloured dots denote particles binned in the phase space r versus λ_z , coloured by their circularity λ_z as shown by the colour bar. The black lines are the same as the upper panels. Note that the y-axis has different scales in the upper and bottom panels.

link between the derived depletion time, and the projected elliptical radius of each bin for the nine mock galaxy projections. In the bottom panels, we show the relation of t_{dep} with the intrinsic radius r for the particles in the simulations, each grey dot represents one particle in the simulation (we plot 1/1000), the coloured dots denote particles binned in the phase space r versus λ_z , coloured by their circularity λ_z as shown by the colour bar.

To correct for the loss of information (primarily the suppression of the width of projected metallicity and age distributions, compared to the true particle distributions), we compute a depletion time correlation with radius that extends to larger values than the (biased) projected bins. We find that a more complete range of depletion times (important for the most metal-poor orbits) is encompassed if we fit a linear relation $t_{\text{dep}}(r) = ar + b$ to two points: (1) $t_{\text{dep, min}}$ based on the observed age and metallicity at $r = 0$, (2) $t_{\text{dep}}(R_e) = 4 \text{ Gyr}$. This relation that we adopt for this work is shown as the black line in Fig. A1. The relations are generally consistent with the relation of t_{dep} with the intrinsic radius r in the simulations.

APPENDIX B: FIGURES FOR ALL NINE GALAXIES

Similar to figures we show for the galaxy Au-6 $\theta = 80^\circ$ in Section 4. Fig. B1 shows the stellar orbit distribution in r versus λ_z comparing with the true from simulation and those from our models for all nine galaxies. Figs B2 and B3 show the stellar population distribution t versus Z from our models for all nine galaxies, with different priors of R1 and R2, respectively. Figs B4 and B5 are the correlation of age t and circularity λ_z for all nine galaxies, with different priors of R1 and R2, respectively.

Similar to figures we show from Au-6 $\theta = 80^\circ$ in Section 5. Fig. B6 are surface brightness, velocity, velocity dispersion, and age and metallicity maps of cold, warm, hot+CR components, comparing with true from simulation with our model R2, for Au-5 $\theta = 80^\circ$ and Au-23 $\theta = 80^\circ$. Fig. B7 is the age and metallicity profiles along major axis.

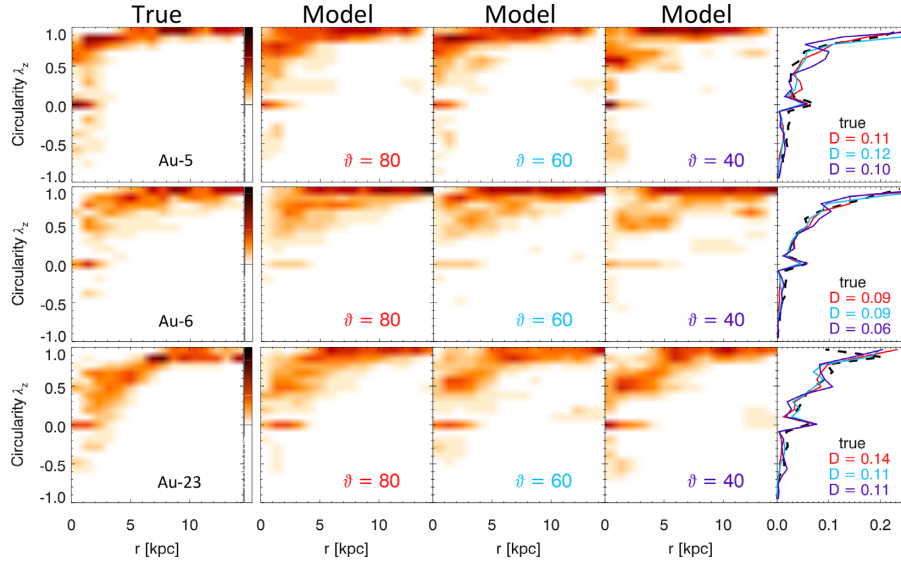


Figure B1. The stellar orbit distribution in λ_z versus r , for Au-5, Au-6, and Au-23 from top to bottom. The first column is the true stellar orbit distributions from simulations. The rest columns are the distribution of orbits in our best-fitting models for mock data with $\vartheta = 80^\circ$, 60° , and 40° from left to right. The last column is the marginalized λ_z distribution. The black dashed curves are the true from simulations; red, blue, and purple solid curves represent those from models for mock data with $\vartheta = 80^\circ$, 60° , and 40° , respectively. The D-statistics D calculated from KS test comparing total λ_z distribution from our model to the true from simulations is labelled with the corresponding colours.

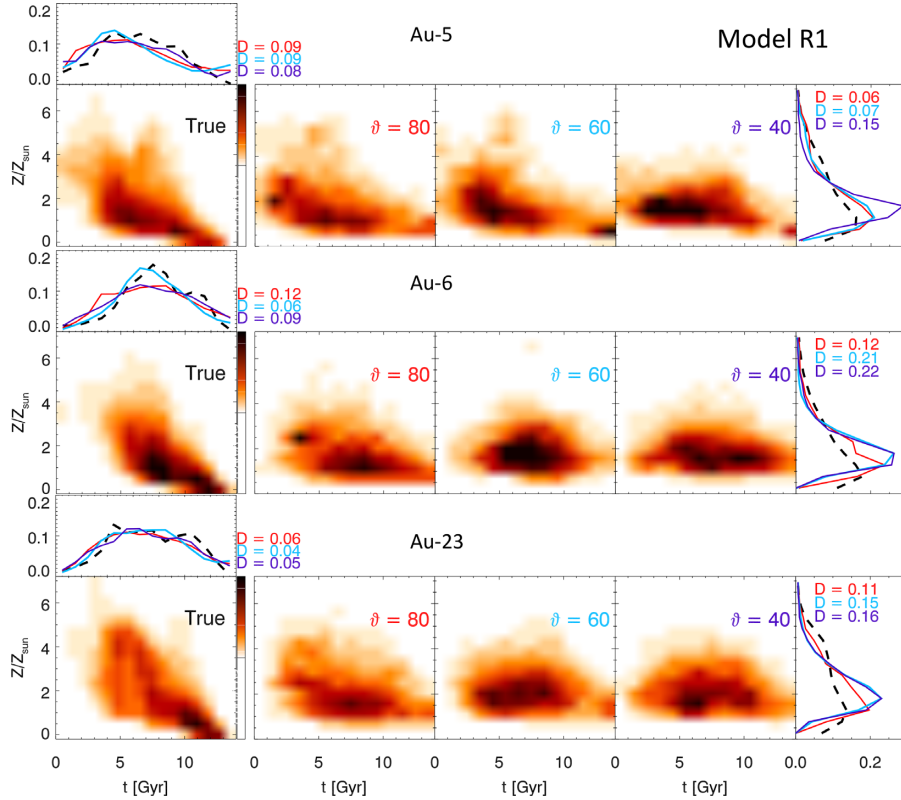


Figure B2. The intrinsic age-metallicity distribution, for Au-5, Au-6, and Au-23 from top to bottom, for model R1. For each halo, the panel labelled with 'True' is the true distribution in age versus Z of particles in the simulation. The following panels from left to right are those obtained by our model for mock data with inclination angle $\vartheta = 80^\circ$, 60° , and 40° , respectively. The contours are smoothed by the distribution of t and Z from MCMC sampling. The upper subpanel is the marginalized age distribution and the right-hand subpanel is the marginalized metallicity Z distribution. The black dashed curve is the true; red, blue, and purple solid curves represent that from model for mock data with $\vartheta = 80^\circ$, 60° , and 40° , respectively, the D-statistics D calculated from 1D KS test is labelled with the corresponding colours.

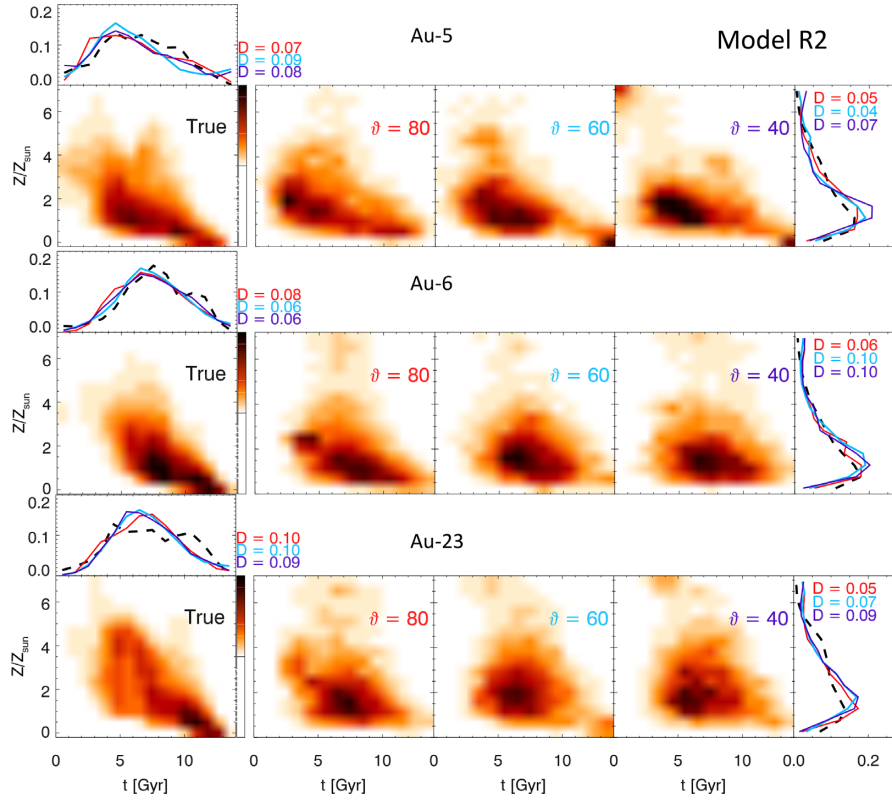


Figure B3. Similar to Fig. B2, but with model R2. The major tracks on age versus metallicity distribution are recovered better than model R1, the D-statistics D from 1D KS test for metallicity distribution is also smaller.

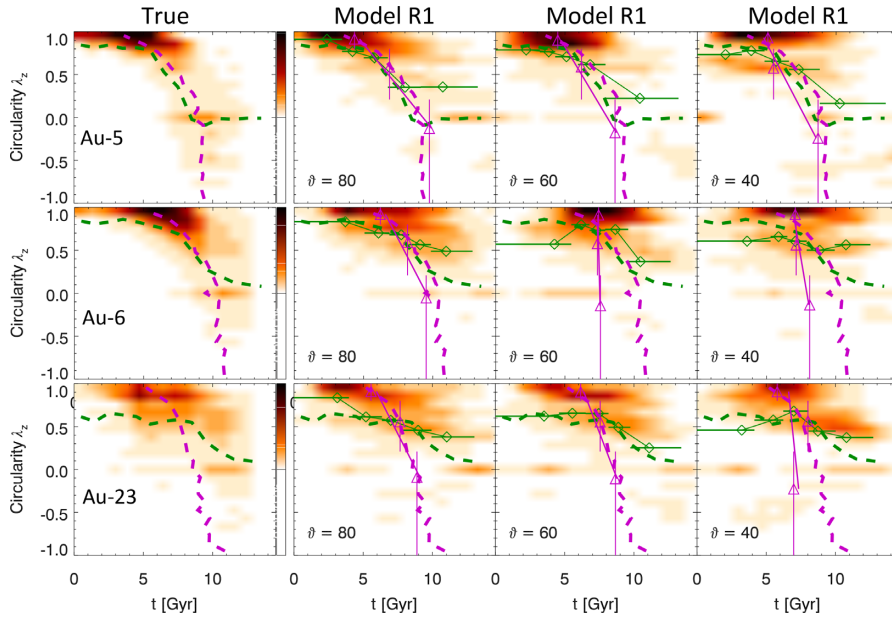


Figure B4. The intrinsic correlation of age versus circularity, for Au-5, Au-6, and Au-23 from top to bottom, for model R1. The first column is true distributions of the particles from simulations, darker colour indicates higher probability density, the magenta dashed curves are average t as a function of λ_z , and the green dashed curves are average λ_z as a function of age t for the true distributions. The following panels from left to right are those obtained by our models for mock data with inclination angle $\vartheta = 80^\circ$, 60° , and 40° , respectively. In each panel, the magenta triangles are average t as a function of λ_z , the magenta lines are linear fits to the triangles, and the green diamonds are average λ_z as a function of age t from the model.

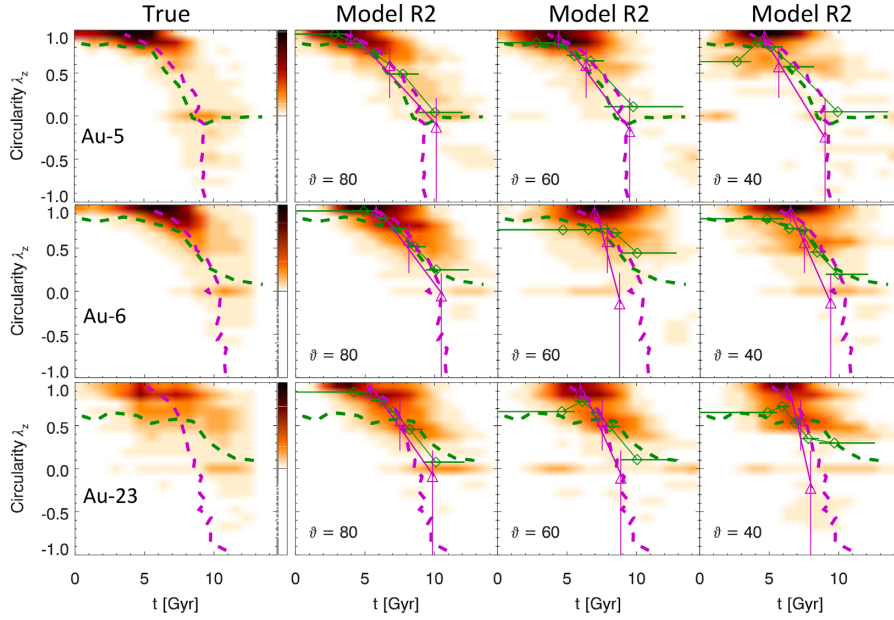


Figure B5. Similar to Fig. B4, but for model R2, in which we use $t = t_0 + p\lambda_z$ (the blue line fitting the blue triangles) from model R1 as priors of t_k in fitting the age map. Model R2 matches the age versus λ_z correlation in the simulation better than model R1, especially for face-on galaxies.

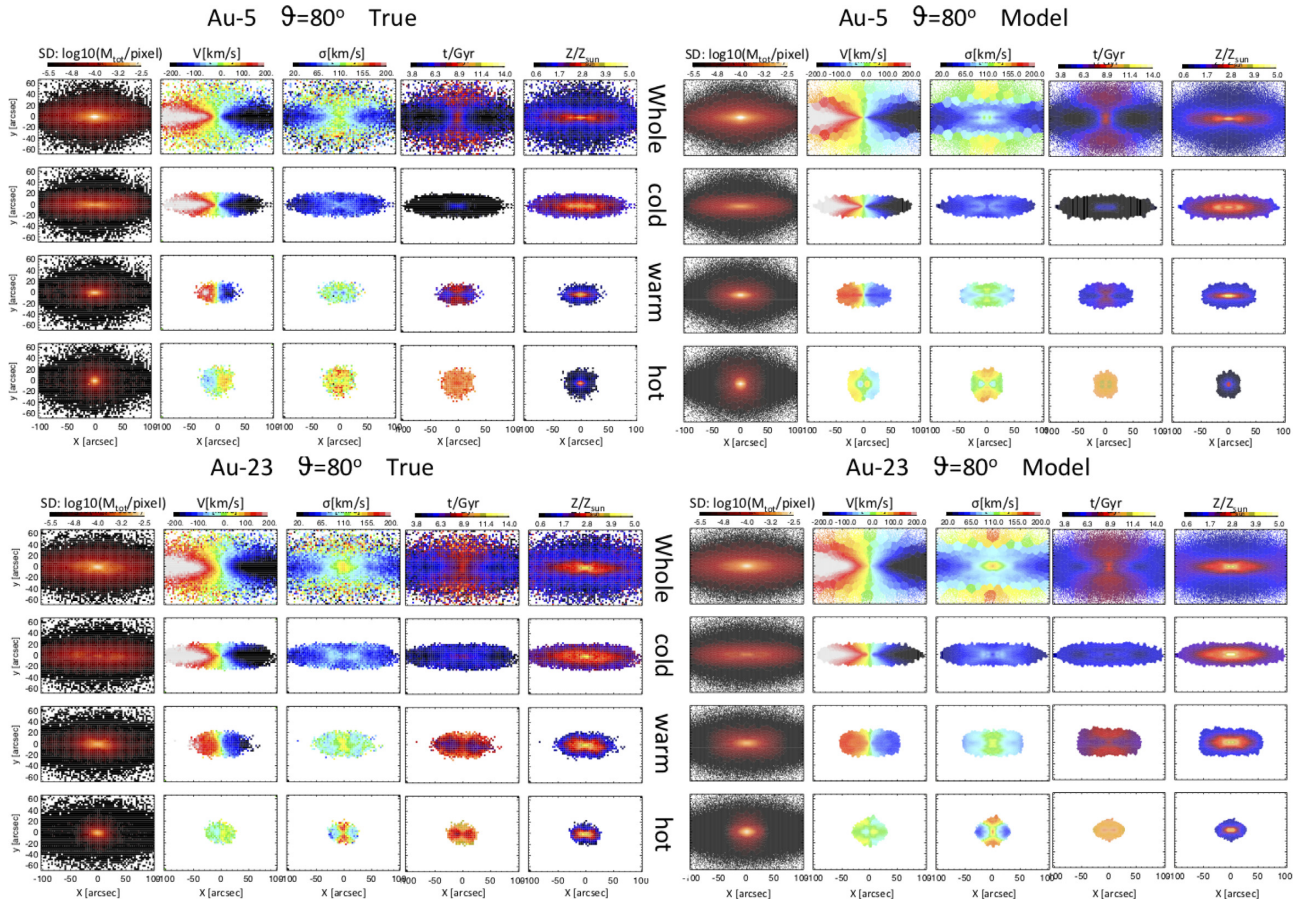


Figure B6. Surface mass density/brightness, velocity, velocity dispersion, and age and metallicity maps of the whole galaxy, cold, warm, and hot+CR component (from top to bottom) of Au-5 $\theta = 80^\circ$ and Au-23 $\theta = 80^\circ$. The left-hand panels are the true values from the simulation, and the right-hand panels are rebuilt by orbital bundles from our model R2. These galaxies are at a distance of 30 Mpc, 1 arcsec = 145 pc.

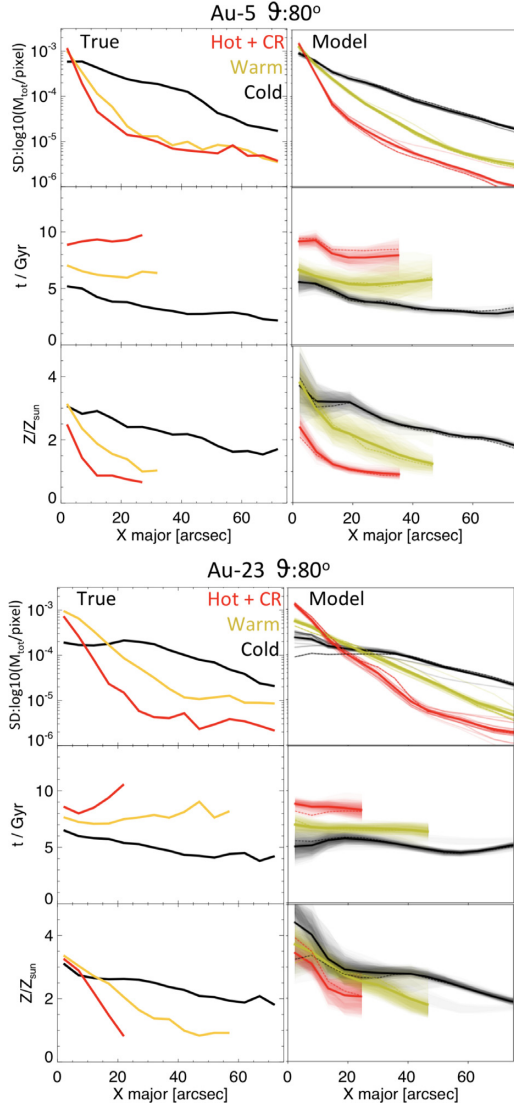


Figure B7. Surface mass density/brightness profile, age, and metallicity along major axis (1 arcsec = 145 pc) of the cold, warm, and hot component, comparison between true and those built by model, similar to Fig. 10 for Au-6 $\vartheta = 80^\circ$. We generally recover the surface brightness, age, and metallicity profiles of each component well. Except for Au-23, we overestimate metallicity of cold component in the inner regions, thus resulting in a stronger negative metallicity gradient of this component than the true.

This paper has been typeset from a \LaTeX file prepared by the author.